J Geophys (1985) 58:125–145

Journal of Geophysics

Synthetic seismograms: the Rayleigh waves modal summation

G.F. Panza

Istituto di Geodesia e Geofisica, Università di Trieste and International School for Advanced Studies, 34100 Trieste, Italy

Abstract. From the latest developments of algorithms for the computation of eigenvalues and eigenfunctions of Rayleigh waves for flat layered anelastic models of the Earth, it is possible to construct, with highly satisfactory efficiency and accuracy, "complete" synthetic seismograms also at high frequencies. Examples are given both for continental and oceanic structural models made up of 70 layers and more and extending to depths of about 1,100 km.

Key words: Synthetic seismograms – Rayleigh modes – Anelasticity

1. Introduction

Pekeris (1948), in his pioneering work, has shown the possibility of treating the problem of wave propagation in homogeneous layered media, both in terms of rays (ray-theory) and in terms of modes (normal mode solution); he also proposed the use of ray theory for the purpose of determining the beginning of the record at a distant point or for determining the steady-state solution up to moderate ranges. On the other hand, if one is interested in the steady-state solution at large ranges where many rays need to be considered, or in the later phases received at large distances, the normal mode solution is preferable. Since Pekeris' paper, a considerable amount of research has been carried out following both approaches. A modern review of the results achieved in the determination of seismic wave propagation in stratified media is given by Kennett (1983).

From Kennett's book it is quite evident that a great concentration of effort to understand the way in which the features of observed seismograms are related to the properties of the source and structure of the Earth is based on a variety of mathematical and physical tools essentially inspired by the ray-theory and its developments.

On the other hand, modal summation has been successfully applied to the generation of synthetic signals only for periods greater than 10 s (e.g. Liao et al., 1978; Cuscito and Panza, 1981; Panza and Cuscito, 1982; Woodhouse, 1983).

It would seem that lack of an explicit statement of the details of high-frequency eigenvalue and eigenfunction evaluation has been the main factor delaying large-scale application of multimode, synthetic seismograms to the interpretation of short-period experimental records. There are essentially two types of computational problems: (a) remove the loss-of-precision contained in the original Thomson (1950) – Haskell (1953) technique for the computation of Rayleigh-wave dispersion; (b) reach the necessary accuracy and efficiency in modal computation at high frequency, where many modes get very close to each other. To deal with the loss-of-precision problem, two methods exist: Knopoff's (1964a) method and the method of delta matrices (Pestel and Leckie, 1963; Thrower, 1965; Dunkin, 1965; Watson, 1970). Very recently, as a result of intensive international cooperation, Schwab et al. (1984) have shown, both for eigenvalue and eigenfunction determinations, that there are no loss-of-precision problems when the existing improvements of the original formulation are used – also for frequencies as high as 10000 Hz. The problem of computational efficiency, while retaining very high accuracy, at short periods has been treated with some success by Suhadolc et al. (1985). Thus, at present, the use of multimode summation for the construction of synthetic seismograms can be extended to high frequencies.

2. Computation of eigenvalues

Knopoff (1964a) has given the solution to problems of elastic wave propagation in multilayered media as the quotient of products of matrices. In the case of SH waves, the matrices are of order two; in the case of $P-SV$ waves the matrices are of order four. The individual matrix elements are themselves determinants of order two or four in the two cases.

Concerning the determination of the Rayleigh-wave phase velocity using Knopoff's method, it was reported (Schwab, 1970) that with 16 decimal digits carried during computation and 15.4 significant figures required in the computed phase velocities, the number of wavelengths of a layered structure above the homogeneous half-space can be increased to 196 without any loss of precision. To control overflow when a large number, H/λ, of wavelengths of layered structure (H is the depth to the deepest interface and λ is the wavelength) is used in the computation, a simple normalization is required (Schwab et al., 1984). With normalization included, so that large values of H/λ can be treated, only the following overflow/underflow situations must be avoided.

The matrix elements for the layers with $c<\beta_m<\alpha_m$, where c is the phase velocity, β_m is the S-wave velocity of the m-th layer and α_m is the P-wave velocity of the m-th layer, contain factors of the form (Schwab, 1970):

$$\begin{matrix}\sinh\\ \cosh\end{matrix} P_m^* \begin{matrix}\sinh\\ \cosh\end{matrix} Q_m^* \tag{1}$$

where

$$\begin{aligned} P_m^* &= -\frac{\omega d_m}{c}\sqrt{1-\frac{c^2}{\alpha_m^2}} = -\frac{\omega d_m}{c} r_{\alpha_m}^* \quad \text{real} \\ Q_m^* &= -\frac{\omega d_m}{c}\sqrt{1-\frac{c^2}{\beta_m^2}} = -\frac{\omega d_m}{c} r_{\beta_m}^* \quad \text{real} \end{aligned} \tag{2}$$

where d_m is the thickness of the m-th layer and ω is the angular frequency. In the notation used here, the asterisk denotes the imaginary part of an imaginary quantity. For large values of the arguments, the magnitude of these factors is approximated by:

$$\frac{1}{4}\exp\left[\frac{\omega d_m}{c}(r_{\alpha_m}^*+r_{\beta_m}^*)\right]. \tag{3}$$

In fact,

$$\begin{aligned} &\sinh P^* = [\exp(P^*) - \exp(-P^*)]/2 \\ &\text{and} \\ &\cosh P^* = [\exp(P^*) + \exp(-P^*)]/2 \end{aligned} \tag{4}$$

which reduces to

$$\sinh P^* \simeq -\exp(-P^*)/2 \qquad \cosh P^* \simeq \exp(-P^*)/2$$

when $P^* \ll 0$; the same for Q^*.

Thus, overflow occurs when the last expression is approximately equal to the maximum value permitted by the computer. Denoting this last quantity as MAX, it is easy to find the limiting values

$$\begin{aligned} (d_m)_{\text{maximum}} &= \frac{c\ln(4\cdot\text{MAX})}{\omega(r_{\alpha_m}^*+r_{\beta_m}^*)} \\ c_{\text{minimum}} &= \frac{\omega d_m(r_{\alpha_m}^*+r_{\beta_m}^*)}{\ln(4\cdot\text{MAX})} \\ \omega_{\text{maximum}} &= \frac{c\ln(4\cdot\text{MAX})}{d_m(r_{\alpha_m}^*+r_{\beta_m}^*)} \end{aligned} \tag{5}$$

to avoid overflow during the evaluation of the matrix elements for any given layer. If these limits are reached, splitting the thick layers into thinner ones having the same properties does not solve the problem (Schwab et al., 1984). A powerful, general solution to the problem of handling homogeneous layers, when they are many wavelengths thick, is the following. When $c<\beta_m<\alpha_m$ and d_m/λ is large, for layer m, it is possible to use the approximation

$$\begin{aligned} \sinh P_m^* &= -\tfrac{1}{2}\exp(k r_{\alpha_m}^* d_m) \\ \cosh P_m^* &= \tfrac{1}{2}\exp(k r_{\alpha_m}^* d_m) \end{aligned} \tag{6}$$

where $k=\omega/c$. The same is valid for $\sinh Q_m^*$ and $\cosh Q_m^*$. It is important to note that these approximated expressions are exact for a finite-precision computer when the magnitudes of P_m^* and Q_m^* increase beyond a certain point. In fact

$$\begin{matrix}\cosh\\ \sinh\end{matrix} x = \tfrac{1}{2}\exp(x) \pm \tfrac{1}{2}\exp(-x). \tag{7}$$

If x increases, reaching the point where

$$\tfrac{1}{2}\exp(-x) = 10^M \tfrac{1}{2}\exp(x), \tag{8}$$

where M is the number of decimal digits carried by the computer, then it is algorithmically exact to use

$$\cosh x = -\sinh x = \tfrac{1}{2}\exp(-x) \qquad x<0. \tag{9}$$

Thus, in Eq. (1) it is possible to factor out the quantity

$$\tfrac{1}{4}\exp[k d_m(r_{\alpha_m}^*+r_{\beta_m}^*)] \tag{10}$$

which is always positive. Since the interest is limited to changes in sign of the dispersion function, this factor can be deleted when treating layer m and consequently there is no more need to deal with exponentials having arguments above a certain level.

The case $\beta_m<c<\alpha_m$ and large d_m/λ can be treated by analogy and it is possible to delete terms like

$$\tfrac{1}{2}\exp(k d_m r_{\alpha_m}^*). \tag{11}$$

The power of this approach has been extensively tested by Schwab et al. (1984) and Suhadolc et al. (1985).

Once the phase velocity, c, is obtained for a given angular frequency ω, the group velocity, u, is obtained from

$$u = c\Bigg/\left(1-\frac{c}{\omega}\frac{dc}{d\omega}\right) \tag{12}$$

where standard implicit function theory is applied to the dispersion function, F, to obtain

$$\frac{dc}{d\omega} = -\left(\frac{\partial F}{\partial\omega}\right)_c \Bigg/ \left(\frac{\partial F}{\partial c}\right)_\omega. \tag{13}$$

For details, see Schwab and Knopoff (1972). From Eq. (12) it is evident that the computation of u requires as input the phase velocity, c. Thus the accuracy with which u can be computed, δu, depends on the accuracy, δc, of c. Extensive tests of such dependence have been carried out by Schwab et al. (1985) who show the existence of a quite general linear relation between δu and δc. Their results show that it is necessary to compute the phase velocity with at least seven significant figures to ensure three significant figures in group velocity. However, as will be shown later, a greater accuracy in c is needed to compute accurate eigenfunctions.

3. Computations of eigenfunctions

The algorithmic details of eigenfunction evaluation with Knopoff's method are rather involved – although in principle only a straightforward application of Cramer's rule is required – whereas the details for the original formulation (Haskell, 1953) are quite simple. Full details concerning Knopoff's method are given by Schwab et al. (1984); here, it is sufficient to remember the following. Using Haskell notation, the displacements – u_m (radial), w_m (vertical) – or equivalently the corresponding velocities $\dot{u}_m$ and $\dot{w}_m$, and the stresses – σ_m (normal), τ_m (tangential) – in the m-th layer are given by:

$$
\begin{aligned}
c\,\dot{u}_m &= A_m \cos p_m - i B_m \sin p_m \\
&\quad + r_{\beta_m} C_m \cos q_m - i r_{\beta_m} D_m \sin q_m, \\
c\,\dot{w}_m &= -i r_{\alpha_m} A_m \sin p_m + r_{\alpha_m} B_m \cos p_m \\
&\quad + i C_m \sin q_m - D_m \cos q_m, \\
\sigma_m &= \rho_m(\gamma_m - 1) A_m \cos p_m - i \rho_m(\gamma_m - 1) \\
&\quad \cdot B_m \sin p_m + \rho_m \gamma_m r_{\beta_m} C_m \cos q_m \\
&\quad - i \rho_m \gamma_m r_{\beta_m} D_m \sin q_m, \\
\tau_m &= i \rho_m \gamma_m r_{\alpha_m} A_m \sin p_m - \rho_m \gamma_m r_{\alpha_m} \\
&\quad \cdot B_m \cos p_m - i \rho_m(\gamma_m - 1) C_m \sin q_m \\
&\quad + \rho_m(\gamma_m - 1) D_m \cos q_m,
\end{aligned}
\tag{14}
$$

Thus Knopoff's submatrix $\Lambda^{(0)}$ can be written in the form

$$
\Lambda^{(0)} = \begin{bmatrix} -\rho_1(\gamma_1 - 1) & 0 & -\rho_1 \gamma_1 & 0 \\ 0 & \rho_1 \gamma_1 & 0 & -\rho_1(\gamma_1 - 1) \end{bmatrix}. \tag{17}
$$

At the m-th interface, the continuity of displacement and stress yields

$$
\begin{aligned}
& A_m \cos P_m - i B_m \sin P_m + r_{\beta_m} C_m \cos Q_m - i r_{\beta_m} D_m \sin Q_m \\
&\quad = A_{m+1} + r_{\beta_{m+1}} C_{m+1}, \\
& -i r_{\alpha_m} A_m \sin P_m + r_{\alpha_m} B_m \cos P_m + i C_m \sin Q_m - D_m \cos Q_m \\
&\quad = r_{\alpha_{m+1}} B_{m+1} - D_{m+1}, \\
& \rho_m(\gamma_m - 1) A_m \cos P_m - i \rho_m(\gamma_m - 1) B_m \sin P_m \\
&\qquad + \rho_m \gamma_m r_{\beta_m} C_m \cos Q_m - i \rho_m \gamma_m r_{\beta_m} D_m \sin Q_m \\
&\quad = \rho_{m+1}(\gamma_{m+1} - 1) A_{m+1} + \rho_{m+1} \gamma_{m+1} r_{\beta_{m+1}} C_{m+1}, \\
& i \rho_m \gamma_m r_{\alpha_m} A_m \sin P_m - \rho_m \gamma_m r_{\alpha_m} B_m \cos P_m \\
&\qquad - i \rho_m(\gamma_m - 1) C_m \sin Q_m + \rho_m(\gamma_m - 1) D_m \cos Q_m \\
&\quad = -\rho_{m+1} \gamma_{m+1} r_{\alpha_{m+1}} B_{m+1} + \rho_{m+1}(\gamma_{m+1} - 1) D_{m+1},
\end{aligned}
\tag{18}
$$

where $P_m = k r_{\alpha_m} d_m$, $Q_m = k r_{\beta_m} d_m$ and d_m is the layer thickness. Thus, Knopoff's 4×8 interface submatrices have the form

$$
\Lambda^{(m)} = \begin{bmatrix}
\cos P_m & -i \sin P_m / r_{\alpha_m} & \cos Q_m & -i r_{\beta_m} \sin Q_m & -1 & 0 & -1 & 0 \\
-i r_{\alpha_m} \sin P_m & \cos P_m & i \sin Q_m / r_{\beta_m} & -\cos Q_m & 0 & -1 & 0 & 1 \\
\rho_m(\gamma_m - 1) \cos P_m & -i \rho_m(\gamma_m - 1) \sin P_m / r_{\alpha_m} & \rho_m \gamma_m \cos Q_m & -i \rho_m \gamma_m r_{\beta_m} \sin Q_m & -\rho_{m+1}(\gamma_{m+1} - 1) & 0 & -\rho_{m+1} \gamma_{m+1} & 0 \\
i \rho_m \gamma_m r_{\alpha_m} \sin P_m & -\rho_m \gamma_m \cos P_m & -i \rho_m(\gamma_m - 1) \sin Q_m / r_{\beta_m} & \rho_m(\gamma_m - 1) \cos Q_m & 0 & \rho_{m+1} \gamma_{m+1} & 0 & -\rho_{m+1}(\gamma_{m+1} - 1)
\end{bmatrix} \tag{19}
$$

where

$$
\begin{aligned}
A_m &= -\alpha_m^2(\Delta'_m + \Delta''_m), & B_m &= -\alpha_m^2(\Delta'_m - \Delta''_m), \\
C_m &= -2\beta_m^2(\omega'_m - \omega''_m), & D_m &= -2\beta_m^2(\omega'_m + \omega''_m), \\
p_m &= k r_{\alpha_m}[z - z^{(m-1)}], & q_m &= k r_{\beta_m}[z - z^{(m-1)}], \\
& & \gamma_m &= 2(\beta_m / c)^2.
\end{aligned}
\tag{15}
$$

ρ_m is the density, $z^{(m-1)}$ is the depth of the upper interface of the m-th layer and Δ'_m, Δ''_m, ω'_m, ω''_m are Haskell (1953) constants appearing in the depth-dependent part of the dilatational and rotational wave solutions:

$$
\Delta'_m \exp(-i k r_{\alpha_m} z) + \Delta''_m \exp(i k r_{\alpha_m} z),
$$

$$
\omega'_m \exp(-i k r_{\beta_m} z) + \omega''_m \exp(i k r_{\beta_m} z).
$$

For a continental model, the vanishing of the two components of stress at the free surface yields:

$$
\begin{aligned}
& -\rho_1(\gamma_1 - 1) A_1 - \rho_1 \gamma_1 r_{\beta_1} C_1 = 0, \\
& \rho_1 \gamma_1 r_{\alpha_1} B_1 - \rho_1(\gamma_1 - 1) D_1 = 0.
\end{aligned}
\tag{16}
$$

and, noting that in the half-space $A_n = B_n = -\alpha_n^2 \Delta'_n$, $C_n = D_n = -2\beta_n^2 \omega'_n$, the submatrix representing the $(n-1)$th interface has the form

$$
\Lambda^{(n-1)} = \begin{bmatrix}
\cdots & -1 & -r_{\beta_n} \\
\cdots & -r_{\alpha_n} & 1 \\
\cdots & -\rho_n(\gamma_n - 1) & -\rho_n \gamma_n r_{\beta_n} \\
\cdots & \rho_n \gamma_n r_{\alpha_n} & -\rho_n(\gamma_n - 1)
\end{bmatrix}, \tag{20}
$$

where the first four columns are the same as those of $\Lambda^{(m)}$ with $m = n - 1$. It may be worth observing here that, for each layer, $\Lambda^{(i)}$ $(i = 1, n)$ submatrices represent the denominators of Cramer's system solutions when the boundary conditions are applied.

Once the phase velocity is determined, the problem of the evaluation of the eigenfunctions reduces to the determination of the constants A_m, B_m, C_m, D_m for the layers and A_n, D_n for the half-space.

Indeed in writing Eq. (19) it was chosen to determine $r_{\alpha_m} B_m$ and $r_{\beta_m} C_m$ instead of B_m and C_m. This choice of the layer constants is particularly convenient since it makes all the elements y_{ij} of Eq. (19), when not equal to zero, real quantities if $i + j$ is even and imaginary quantities if $i + j$ is odd. The starting point is therefore the linear, homogeneous system of $4n - 2$ equations in $4n - 2$ unknowns (Schwab et al., 1984):

$$
\begin{bmatrix}
\boxed{A^{(0)}} & & & & \\
& \boxed{A^{(1)}} & & & \\
& & \ddots & & \\
& & & \boxed{A^{(n-2)}} & \\
& & & & \boxed{A^{(n-1)}}
\end{bmatrix}
\begin{bmatrix}
A_1 \\ r_{\alpha_1} B_1 \\ r_{\beta_1} C_1 \\ D_1 \\ A_2 \\ r_{\alpha_2} B_2 \\ r_{\beta_2} C_2 \\ D_2 \\ \vdots \\ A_{n-1} \\ r_{\alpha_{n-1}} B_{n-1} \\ r_{\beta_{n-1}} C_{n-1} \\ D_{n-1} \\ A_n \\ D_n
\end{bmatrix}
=
\begin{bmatrix}
0 \\ \\ \\ \\ \\ \\ \\ \\ \vdots \\ \\ \\ \\ \\ \\ 0
\end{bmatrix}, \quad (21)
$$

The determination of the layer constants can be started by deleting the last equation of the system and transposing the terms containing D_n to the right-hand side of the equations, thus forming a vector of inhomogeneous terms.

Furthermore, D_n can be arbitrarily set equal to 1; as a consequence $r_{\alpha_m} B_m$ and D_m will be real, while A_m and $r_{\beta_m} C_m$ will be imaginary. Thus the system can be written as:

$$
\begin{bmatrix}
\quad & & \quad \\
& & \\
& &
\end{bmatrix}
\begin{bmatrix}
A_1 \\ \vdots \\ r_{\alpha_{n-1}} B_{n-1} \\ r_{\beta_{n-1}} C_{n-1} \\ D_{n-1} \\ A_n
\end{bmatrix}
=
\begin{bmatrix}
0 \\ \vdots \\ 0 \\ r_{\beta_n} \\ -1 \\ \rho_n \gamma_n r_{\beta_n}
\end{bmatrix}
\quad (22)
$$

from which A_n can be determined.

To obtain A_{n-1}, $r_{\alpha_{n-1}} B_{n-1}$, $r_{\beta_{n-1}} C_{n-1}$, D_{n-1}, Eq. (22) is further reduced by deleting the last equation of the system and transposing terms including A_n to the right-hand side of the equations:

$$
\begin{bmatrix}
\quad & & \quad \\
& & \\
& &
\end{bmatrix}
\begin{bmatrix}
A_1 \\ \vdots \\ A_{n-1} \\ r_{\alpha_{n-1}} B_{n-1} \\ r_{\beta_{n-1}} C_{n-1} \\ D_{n-1}
\end{bmatrix}
=
\begin{bmatrix}
0 \\ \vdots \\ 0 \\ \psi_1(n) \\ \psi_2(n)
\end{bmatrix}
\quad (23)
$$

where $\psi_1(n) = A_n + r_{\beta_n}$ Imaginary

$\psi_2(n) = r_{\alpha_n} A_n - 1$ Real.

This procedure can be continued to obtain the remaining layer constants, with the only change being in the definition of the two elements of the vector of inhomogeneities:

$$
\left.\begin{aligned}
\psi_1(m) &= A_m + r_{\beta_m} C_m \\
\psi_2(m) &= r_{\alpha_m} B_m - D_m
\end{aligned}\right\} \quad m < n.
$$

For more computational details, see Schwab et al. (1984).

4. Energy integral

In multimode synthesis of theoretical seismograms, the following integral of eigenfunctions must be computed:

$$I_1 = \int_0^\infty \rho(z) [y_1^2(z) + y_3^2(z)] \, dz, \quad (24)$$

where

$$y_1 = \frac{w(z)}{w(0)} = \frac{\dot{w}(z)}{\dot{w}(0)}$$

$$i y_3 = \frac{u(z)}{w(0)} = \frac{\dot{u}(z)}{\dot{w}(0)}$$

which is usually called the energy integral. For a sequence of homogeneous layers, this integral can be evaluated analytically from the layer constants (Schwab et al., 1984).

5. Attenuation due to anelastically

The anelastic nature of the Earth's interior manifests itself through the phenomena of attenuation of elastic waves. Knopoff (1964b) introduced an additional term into the differential equation of motion to account for attenuation effects. He introduced the nondimensional constant Q, which is related to the space ($e^{-\alpha x}$) and time ($e^{-\gamma t}$) attenuation coefficients as follows

$$\alpha = \frac{\omega}{2Qc} \qquad \gamma = \frac{\omega}{2Q} \quad (25)$$

where c is the phase velocity of the plane wave motion under consideration.

Recently, O'Connell and Budiansky (1978) derived the relation

$$Q = \frac{1}{2} \left(\frac{\omega}{\alpha c} - \frac{\alpha c}{\omega} \right) \quad (26)$$

which is relevant only for small values of ω (long-period waves and free oscillations). Brune (1962) and Knopoff et al. (1964) noted that there are some discrepancies for Q obtained from propagating wave trains, Q_x, and that from free oscillations, Q_t. The two values are joined by the relation $u Q_t = c Q_x$ where c and u are phase and group velocity, respectively.

Attenuation also distorts dispersion properties. Futterman (1962) pointed out that physical dispersion must accompany wave attenuation to preserve causality principle. In a medium with a constant Q, the correction to the dispersion of body waves can be expressed

$$
\begin{aligned}
A_1(\omega) &= A_1(\omega_0) \Big/ \left\{ 1 + \left[\frac{2}{\pi} A_1(\omega_0) A_2(\omega_0) \ln(\omega_0/\omega) \right] \right\}, \\
B_1(\omega) &= B_1(\omega_0) \Big/ \left\{ 1 + \left[\frac{2}{\pi} B_1(\omega_0) B_2(\omega_0) \ln(\omega_0/\omega) \right] \right\},
\end{aligned}
\quad (27)
$$

where $A_1(\omega)$ is the P-wave phase velocity, $A_2(\omega)$ is the P-wave phase attenuation, $B_1(\omega)$ is the S-wave phase velocity and $B_2(\omega)$ is the S-wave phase attenuation.

In the following computations we have choosen $\omega_0 = 2\pi$ radians. The quantities A_1, A_2, B_1, B_2 are related to the complex body-wave velocities α and β, describing the properties of anelastic media, by

$$\frac{1}{\alpha}=\frac{1}{A_1}-i A_2, \quad \frac{1}{\beta}=\frac{1}{B_1}-i B_2 \tag{28}$$

(Schwab and Knopoff, 1972). In anelastic media also surface-wave phase velocity. c, must be expressed as a complex quantity

$$\frac{1}{c}=\frac{1}{C_1}-i C_2. \tag{29}$$

The attenuated phase velocity C_1 and the phase attenuation C_2 can be estimated by using the variational technique (e.g. Takeuchi and Saito, 1972; Aki and Richards, 1980). As an intermediate step it is necessary to compute the integrals

$$I_3=\int_0^\infty \left\{\left[(\lambda+2\mu)-\frac{\lambda^2}{(\lambda+2\mu)}\right] y_3^2 + \frac{1}{k}\left(y_1 y_4-\frac{\lambda}{(\lambda+2\mu)} y_2 y_3\right)\right\} dz \tag{30}$$

$$I_4=\int_0^\infty \left\{\delta(\lambda+2\mu)\left[\frac{1}{(\lambda+2\mu)^2}(y_2^2+2k\lambda y_2 y_3) + k^2\left(1+\frac{\lambda^2}{(\lambda+2\mu)^2}\right) y_3^2\right] + \delta\mu\frac{1}{\mu^2} y_4^2+\delta\lambda\left[\frac{2k}{(\lambda+2\mu)}(y_2 y_3+k\lambda y_3^2)\right]\right\} dz, \tag{31}$$

where y_1 and y_3 are defined as in Sect. 4,

$$y_2=\frac{\sigma(z)}{w(0)}, \quad i y_4=\frac{\tau(z)}{w(0)},$$

$$\delta\mu=\rho(\beta_1^2-\beta_2^2-\bar{\beta}^2)+i 2\rho\beta_1\beta_2,$$

$$\delta\lambda=\rho[(\alpha_1^2-\alpha_2^2-\bar{\alpha}^2)-2(\beta_1^2-\beta_2^2-\bar{\beta}^2)] + i\rho 2(\alpha_1\alpha_2-2\beta_1\beta_2),$$

$$\delta(\lambda+2\mu)=\rho(\alpha_1^2-\alpha_2^2-\bar{\alpha}^2)+i 2\rho\alpha_1\alpha_2.$$

In these expressions, $\bar{\alpha}$ and $\bar{\beta}$ are the compressional- and shear-wave velocities in the perfectly elastic case; in other words

$$\rho(\beta_1+i\beta_2)^2=\mu+\delta\mu \qquad \rho(\alpha_1+i\alpha_2)^2=(\lambda+2\mu)+\delta(\lambda+2\mu),$$

with λ and μ indicating Lamé's constants.

Integrals I_3 and I_4 can be computed analytically from the layer constants (Schwab et al., 1985), thus obtaining the anelastic phase velocity

$$C_1=\bar{c}\Big/\left[1-\frac{1}{2\bar{k}^2 I_3}\operatorname{Re}(I_4)\right] \tag{32}$$

and the phase attenuation

$$C_2=\frac{1}{2\omega\bar{k} I_3}\operatorname{Im}(I_4), \tag{33}$$

where $\bar{c}$ and $\bar{k}$ are the phase velocity and wavenumber in the perfectly elastic case.

The exact mathematical treatment of attenuation due to anelasticity is described by Schwab and Knopoff (1971, 1972, 1973). Its extension to efficient multimode computation is presently in progress.

6. Examples of computations

The construction of realistic seismograms requires the possibility of handling Earth models formed by a large number of layers including low-velocity zones. Accordingly, with the more recent models of the crust and upper mantle these layers correspond to sedimentary layers, to the laccolithic zone of granitic intrusion (sialic low-velocity zone), to granulitic layers (lower crustal layer) and to the asthenospheric low-velocity layer (e.g. Mueller, 1977; Panza, 1980).

The presence of such velocity inversions removes from the phase velocity spectra (multimode phase velocities) regularities sometimes used (e.g. Kerry, 1981) to approach the multimode summation in an approximated way.

In what follows, examples of exact computations are described for a continental and an oceanic structure containing low-velocity layers both in the crust and in the upper mantle (see Table 1 and Fig. 1).

As can be seen from Table 1, structural properties are specified down to depths of about 1,100 km, where the S-wave velocity reaches 6.42 km/s. The possibility of handling structural models extending to these depths, in an efficient way, makes it possible to synthesize early P-wave arrivals from all crustal layers having a P-wave velocity less than 6.42 km/s; without the necessity of introducing any unrealistic high-velocity half-space, with the consequent generation of spurious S-wave arrivals as, for instance, in the case of the locked mode approximation (Harvey, 1981).

6.1. *Phase velocities*

The Rayleigh-wave dispersion curves for the first 214 modes for the continental model are shown in Fig. 2. It is easy to see the effect of the major discontinuities, present in the structure, which are responsible for all the "quasi-osculations". The standard sequence channel-waves crustal-waves (Panza et al., 1972), due to the presence of the asthenospheric low-velocity layer, is intersected by a family of waves mainly sampling the waveguide formed by the sedimentary layers (Chiaruttini et al., 1985). This is the reason for the quite complicated pattern visible at frequencies larger than 0.1 Hz for phase velocities in the range 4.3–6.3 km/s. Only ten higher modes reach velocities less than 4.3 km/s (the S-wave in the asthenospheric low-velocity layer). When this happens, the modes are essentially sampling only crust. In fact, crustal layering begins to be visible in the phase-velocity curves for frequencies larger than about 0.4 Hz, even if not in the form of "quasi-osculations". This means that to get detailed crustal information it is necessary to reach frequencies much larger than 1 Hz.

Figure 3 shows the Rayleigh-wave dispersion curves for the oceanic model. Here the standard channel-wave crustal-wave sequence is limited to a smaller number of modes because of the presence of a thinner crust. It is also interesting to note that, in addition to the family

Table 1.

Input flat continental structure – IMP1

Depth to interface (km)	Layer thickness (km)	Density (g/cm^3)	P-wave phase velocity (km/s)	P-wave phase attenuation (10^{-5} s/km)	S-wave phase velocity (km/s)	S-wave phase attenuation (10^{-4} s/km)	Q_β	Layer number
0.00	0.10	2.04	1.69	591.70	0.50	500.00	20	1
0.10	0.15	2.06	1.79	558.70	0.82	305.63	20	2
0.25	0.50	2.13	2.17	461.50	1.01	247.50	20	3
0.75	0.50	2.21	2.53	263.20	1.20	138.90	30	4
1.25	0.50	2.28	2.90	172.40	1.41	88.65	40	5
1.75	0.50	2.35	3.27	122.40	1.62	61.73	50	6
2.25	0.50	2.43	3.63	110.10	1.85	54.05	50	7
2.75	0.50	2.50	4.00	50.00	2.08	24.04	100	8
3.25	0.50	2.57	4.37	30.53	2.33	14.31	150	9
3.75	0.50	2.65	4.73	21.33	2.59	9.65	200	10
4.25	0.50	2.72	5.10	15.69	2.87	6.97	250	11
4.75	0.50	2.77	5.38	12.40	3.06	5.45	300	12
5.25	0.50	2.83	5.65	10.11	3.26	4.38	350	13
5.75	0.25	2.85	5.75	7.73	3.32	3.35	450	14
6.00	0.50	2.85	5.75	7.73	3.32	3.35	450	15
6.50	0.50	2.85	5.75	7.73	3.32	3.35	450	16
7.00	0.50	2.85	5.75	7.73	3.32	3.35	450	17
7.50	0.50	2.85	5.75	7.73	3.32	3.35	450	18
8.00	0.50	2.85	5.75	7.73	3.32	3.35	450	19
8.50	0.50	2.85	5.75	7.73	3.32	3.35	450	20
9.00	0.50	2.85	5.75	7.73	3.32	3.35	450	21
9.50	0.50	2.85	5.75	7.73	3.32	3.35	450	22
10.00	0.50	2.85	5.75	7.73	3.32	3.35	450	23
10.50	0.50	2.85	5.75	7.73	3.32	3.35	450	24
11.00	0.30	3.04	6.70	6.63	3.87	2.87	450	25
11.30	0.30	3.08	6.90	6.44	3.98	2.79	450	26
11.60	0.30	3.12	7.10	6.26	4.10	2.71	450	27
11.90	1.10	3.16	7.30	6.09	4.21	2.64	450	28
13.00	2.00	3.16	7.30	6.09	4.21	2.64	450	29
15.00	2.00	3.16	7.30	6.09	4.21	2.64	450	30
17.00	2.00	3.16	7.30	6.09	4.21	2.64	450	31
19.00	2.00	3.16	7.30	6.09	4.21	2.64	450	32
21.00	2.00	3.16	7.30	6.09	4.21	2.64	450	33
23.00	2.00	3.16	7.30	6.09	4.21	2.64	450	34
25.00	25.00	3.26	7.80	5.70	4.50	2.47	450	35
50.00	25.00	3.40	8.00	25.00	4.30	11.63	100	36
75.00	25.00	3.41	8.00	25.00	4.30	11.63	100	37
100.00	25.00	3.42	8.00	25.00	4.30	11.63	100	38
125.00	25.00	3.43	8.00	25.00	4.30	11.63	100	39
150.00	25.00	3.44	8.00	25.00	4.30	11.63	100	40
175.00	25.00	3.45	8.00	25.00	4.30	11.63	100	41
200.00	25.00	3.46	8.57	15.69	4.60	7.25	150	42
225.00	25.00	3.46	8.57	15.69	4.60	7.25	150	43
250.00	20.00	3.47	8.60	15.50	4.70	7.09	150	44
270.00	20.00	3.47	8.60	15.50	4.70	7.09	150	45
290.00	25.00	3.47	8.70	15.33	4.75	7.02	150	46
315.00	25.00	3.47	8.70	15.33	4.75	7.02	150	47
340.00	25.00	3.47	8.70	15.33	4.75	7.02	150	48
365.00	25.00	3.47	8.70	15.33	4.75	7.02	150	49
390.00	25.00	3.66	8.74	15.15	4.75	6.97	151	50
415.00	20.00	3.88	8.76	15.11	4.75	6.97	151	51
435.00	10.00	3.90	9.04	14.65	5.00	6.61	151	52
445.00	20.00	3.92	9.49	13.95	5.25	6.30	151	53
465.00	25.00	3.93	9.50	13.94	5.25	6.29	151	54
490.00	25.00	3.95	9.52	13.91	5.26	6.29	151	55
515.00	25.00	3.96	9.53	13.90	5.26	6.29	151	56
540.00	25.00	3.99	9.58	13.83	5.29	6.26	151	57
565.00	25.00	4.02	9.63	13.75	5.31	6.23	151	58
590.00	25.00	4.06	9.68	13.67	5.34	6.20	151	59
615.00	25.00	4.09	9.74	12.50	5.37	5.65	165	60
640.00	25.00	4.12	9.78	10.40	5.39	4.73	196	61
665.00	25.00	4.17	10.01	8.80	5.52	3.99	227	62

Table 1. (continued)

Depth to interface (km)	Layer thickness (km)	Density (g/cm^3)	*P*-wave phase velocity (km/s)	*P*-wave phase attenuation (10^{-5} s/km)	*S*-wave phase velocity (km/s)	*S*-wave phase attenuation (10^{-4} s/km)	Q_β	Layer number
690.00	25.00	4.21	10.18	7.61	5.63	3.44	258	63
715.00	25.00	4.26	10.19	6.81	5.75	3.02	288	64
740.00	25.00	4.30	10.49	5.96	5.85	2.68	319	65
765.00	25.00	4.48	10.68	5.35	5.95	2.40	350	66
790.00	25.00	4.63	10.85	4.84	6.04	2.17	381	67
815.00	25.00	4.80	11.03	4.41	6.14	1.98	411	68
840.00	25.00	4.94	11.18	4.05	6.23	1.82	441	69
865.00	25.00	4.94	11.22	3.77	6.25	1.69	473	70
890.00	25.00	4.95	11.27	3.52	6.28	1.58	504	71
915.00	25.00	4.95	11.31	3.31	6.30	1.49	533	72
940.00	25.00	4.95	11.35	3.12	6.32	1.40	565	73
965.00	25.00	4.95	11.39	2.95	6.34	1.32	597	74
990.00	25.00	4.95	11.43	2.79	6.36	1.26	624	75
1015.00	25.00	4.96	11.48	2.65	6.38	1.19	659	76
1040.00	25.00	4.96	11.52	2.52	6.39	1.14	686	77
1065.00	25.00	4.96	11.56	2.41	6.41	1.09	716	78
1090.00	Infinite	4.96	11.60	2.30	6.42	1.04	749	79
Inpunt flat oceanic structure – OCEAN								
0.00	5.00	1.03	1.52					0
5.00	1.00	2.10	2.10	190.48	1.00	100.00	50	1
6.00	2.00	3.07	6.41	49.92	3.70	21.62	62	2
8.00	2.00	3.07	6.41	49.92	3.70	21.62	62	3
10.00	1.00	3.07	6.41	49.92	3.70	21.62	62	4
11.00	1.00	3.40	8.11	9.86	4.61	4.34	250	5
12.00	4.00	3.40	8.11	9.86	4.61	4.34	250	6
16.00	4.00	3.40	8.11	9.86	4.61	4.34	250	7
20.00	1.50	3.40	8.12	9.85	4.61	4.34	250	8
21.50	3.50	3.40	8.12	9.85	4.61	4.34	250	9
25.00	1.50	3.40	8.12	9.85	4.61	4.34	250	10
26.50	5.00	3.40	8.12	9.85	4.61	4.34	250	11
31.50	5.00	3.40	8.12	9.85	4.61	4.34	250	12
36.50	2.50	3.40	8.12	9.85	4.61	4.34	250	13
39.00	1.00	3.40	8.12	9.85	4.61	4.34	250	14
40.00	1.00	3.37	8.01	19.98	4.56	8.77	125	15
41.00	4.00	3.37	8.01	19.98	4.56	8.77	125	16
45.00	5.00	3.37	8.01	19.98	4.56	8.77	125	17
50.00	10.00	3.37	8.01	19.98	4.56	8.77	125	18
60.00	10.00	3.37	7.95	20.13	4.56	8.77	125	19
70.00	10.00	3.37	7.95	20.13	4.56	8.77	125	20
80.00	10.00	3.37	7.71	20.75	4.40	9.09	125	21
90.00	10.00	3.37	7.71	20.75	4.40	9.09	125	22
100.00	20.00	3.33	7.68	20.83	4.34	9.22	125	23
120.00	20.00	3.33	7.78	20.57	4.34	9.22	125	24
140.00	20.00	3.33	7.85	20.83	4.34	9.22	125	25
160.00	20.00	3.33	8.10	19.75	4.45	8.99	125	26
180.00	20.00	3.33	8.12	19.70	4.45	8.99	125	27
200.00	20.00	3.33	8.12	19.70	4.45	8.99	125	28
220.00	20.00	3.33	8.12	19.70	4.45	8.99	125	29
240.00	20.00	3.33	8.12	19.70	4.45	8.99	125	30
260.00	20.00	3.35	8.12	19.70	4.45	8.99	125	31
280.00	20.00	3.36	8.12	19.70	4.45	8.99	125	32
300.00	20.00	3.37	8.12	19.70	4.45	8.99	125	33
320.00	20.00	3.38	8.12	19.70	4.45	8.99	125	34
340.00	20.00	3.39	8.24	19.42	4.50	8.89	125	35
360.00	10.00	3.44	8.30	18.54	4.53	8.49	130	36
370.00	20.00	3.50	8.36	17.72	4.56	8.12	135	37
390.00	5.00	3.68	8.75	16.33	4.61	7.75	140	38
395.00	20.00	3.68	8.75	16.33	4.80	7.45	140	39
415.00	10.00	3.88	9.15	15.07	5.04	6.84	145	40
425.00	10.00	3.88	9.15	14.57	5.04	6.61	150	41
435.00	10.00	3.90	9.43	13.68	5.22	6.18	155	42
445.00	20.00	3.92	9.76	12.81	5.40	5.79	160	43

Table 1. (continued)

Depth to interface (km)	Layer thickness (km)	Density (g/cm³)	*P*-wave phase velocity (km/s)	*P*-wave phase attenuation (10^{-5} s/km)	*S*-wave phase velocity (km/s)	*S*-wave phase attenuation (10^{-4} s/km)	Q_β	Layer number
465.00	25.00	3.93	9.77	12.41	5.40	5.61	165	44
490.00	25.00	3.95	9.78	12.04	5.40	5.45	170	45
515.00	25.00	3.96	9.78	12.03	5.40	5.45	170	46
540.00	25.00	3.99	9.78	12.02	5.40	5.45	170	47
565.00	25.00	4.02	9.79	12.02	5.40	5.45	170	48
590.00	25.00	4.06	9.79	12.02	5.40	5.45	170	49
615.00	25.00	4.09	9.80	12.01	5.40	5.45	170	50
640.00	25.00	4.12	9.80	10.47	5.40	4.75	195	51
665.00	25.00	4.16	10.16	8.20	5.60	3.72	240	52
690.00	25.00	4.21	10.49	6.69	5.80	3.02	285	53
715.00	25.00	4.26	10.82	5.60	6.10	2.48	330	54
740.00	25.00	4.30	11.12	4.80	6.20	2.15	375	55
765.00	25.00	4.48	11.14	4.28	6.21	1.92	420	56
790.00	25.00	4.63	11.15	3.86	6.21	1.73	465	57
815.00	25.00	4.80	11.17	3.55	6.22	1.59	505	58

The rest as for structure IPM1

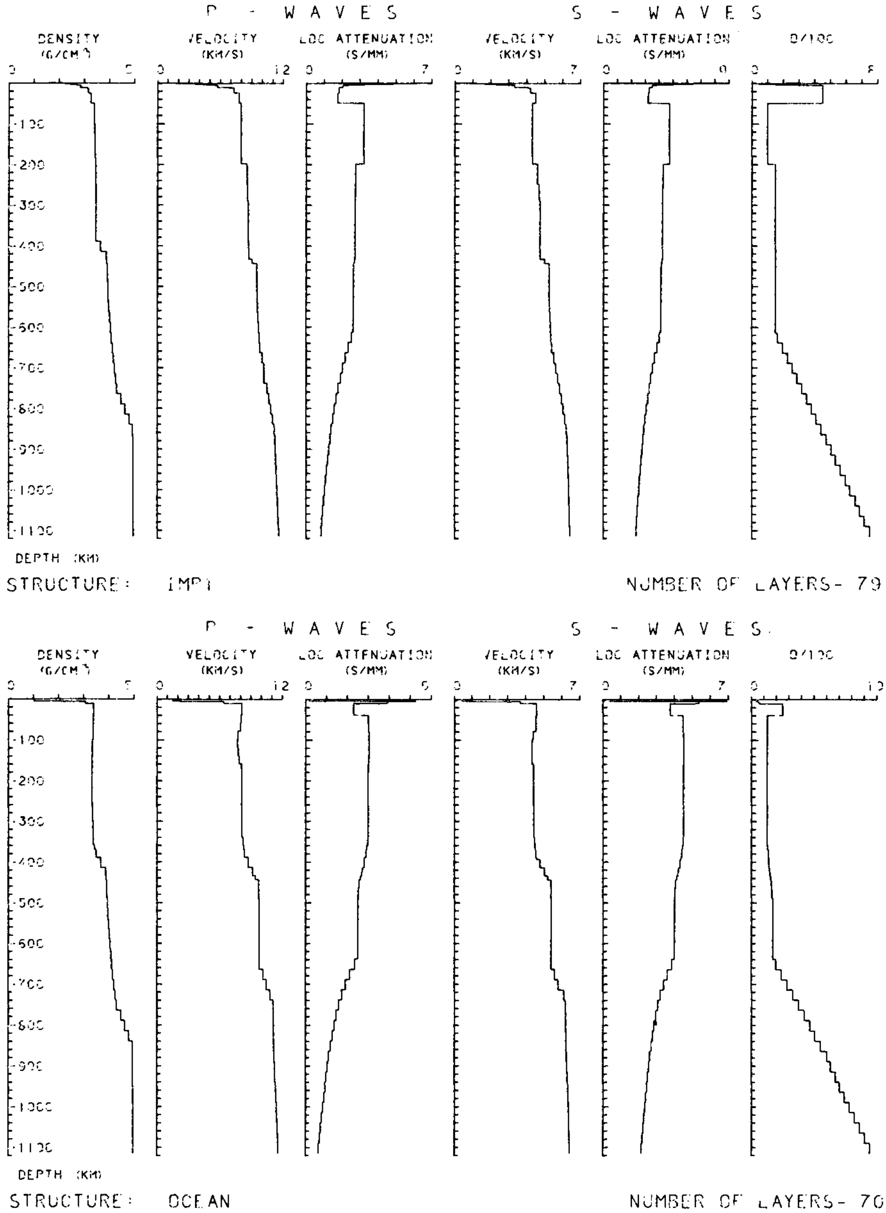

Fig. 1. Distribution versus depth of elastic and anelastic properties for the two structural models used in the computation: IMP1 is the continental structure, OCEAN is the oceanic structure (see also Table 1)

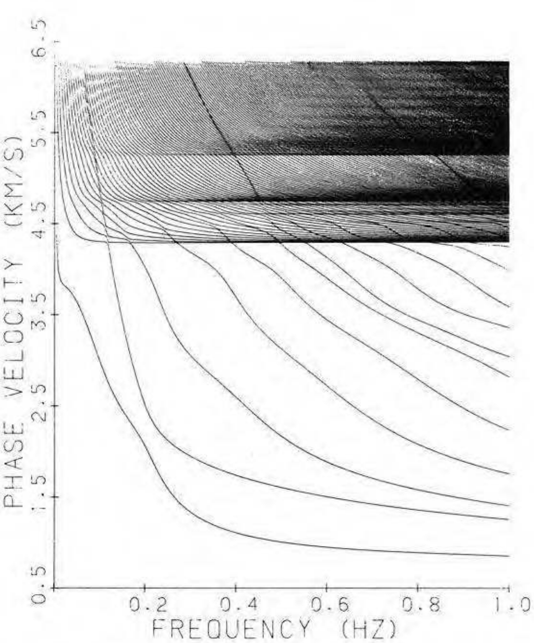

Fig. 2. Rayleigh-wave dispersion curves for the continental structure. Mode numbering is the following: 0 for the fundamental mode, 1 for the first higher mode, 2 for the second higher mode and so on

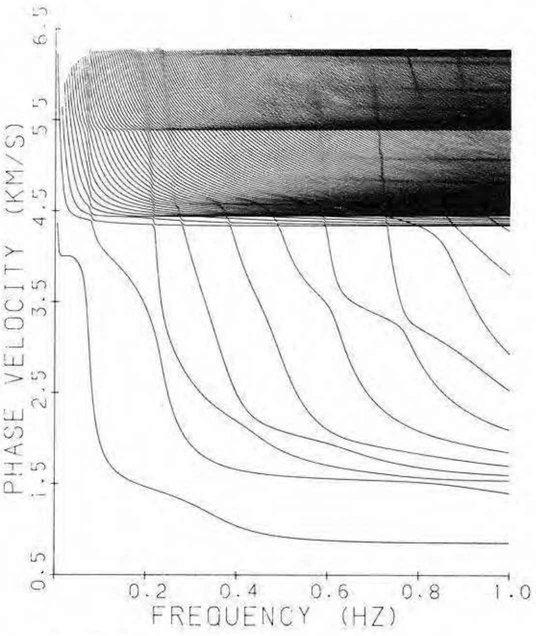

Fig. 3. Rayleigh-wave dispersion curves for the oceanic structure

of waves essentially sampling the sedimentary layers (sedimentary waves), waves mainly propagating in the water layer (water waves) are also visible (Chiaruttini et al., 1985). As in the case of the continental model, the effect of these low-velocity layers is visible also for phase velocities exceeding 6.0 km/s. Also for this model, only ten higher modes are sampling only the crust, i.e. are characterized by phase velocities less than about 4.3 km/s (4.34 km/s is the minimum *S*-wave velocity in the asthenosphere channel). However, the main crustal discontinuities can be easily seen in the dispersion curves.

A common feature of Figs. 2 and 3 is the progressive reduction of the spacing between modes as frequency increases. Since at the same frequency the difference in phase velocities of two adjacent modes can be of the order of 10^{-5} km/s, phase velocities must be computed with an accuracy of more than six figures. This is not a difficult task if use is made of the algorithms previously mentioned, but it is impossible to reach the required accuracy if approximated methods are used in the computation of phase velocities. As will be shown below, to have accurate determination of the eigenfunctions, an even higher accuracy is required in the determination of the phase velocity.

6.2. Group velocities

The group velocities for the two models are shown in Fig. 4 (continental) and Fig 5 (oceanic). Due to the complexity of the pattern it is useless to plot all modes in a single figure, this is why the group-velocity diagram has been subdivided into four parts. Figure 4a gives the first 31 modes. Though it is practically impossible to follow individual modes in their entirety, it is relatively easy to follow the behaviour of channel and crustal waves as well as that of the sedimentary waves for frequencies larger than about 0.09 Hz. The stationary phases formed by the combination of several higher modes, visible in the group velocity interval 2.8–3.7 km/s and starting from frequencies of the order of 0.15 Hz, correspond to *Li* and *Lg* phases (e.g. see Panza and Calcagnile, 1974); while the stationary phases with group velocity around 2.0 km/s and visible for frequencies larger than about 0.2 Hz, correspond to waves essentially propagating in the low-velocity sediments. For group velocities around 2.3–2.5 km/s, stationary phases are visible at frequencies larger than 0.55 Hz; these phases can be associated with waves propagating near the bottom of the sediments.

For frequencies larger than 0.1 Hz and for group velocities around 4.3 km/s, the trapping in the upper-mantle low-velocity layer is clearly visible – being responsible for the very flat portions of the group-velocity curves. Since the *S*-wave velocity in the channel is 4.3 km/s, the *Sa* phase can be identified with the stationary phases centered around group-velocity values of about 4.3 km/s for frequencies less than 0.1 Hz. This interpretation of *Sa*, as a phase mainly controlled by the elastic properties of the first 400 km or so of the Earth's interior, was given by Calcagnile and Panza (1974). For frequencies larger than 0.1 Hz, different branches of *Sn* waves are clearly visible; the fastest tending to a group velocity of about 4.75 km/s (the *S*-wave velocity in the subchannel), the slowest tending to 4.50 km/s (the *S*-wave velocity in the lid). Around a group velocity of 3.9–4.0 km/s, very wide stationary portions are visible for frequencies larger than about 0.4 Hz; they can be associated with *Sb*

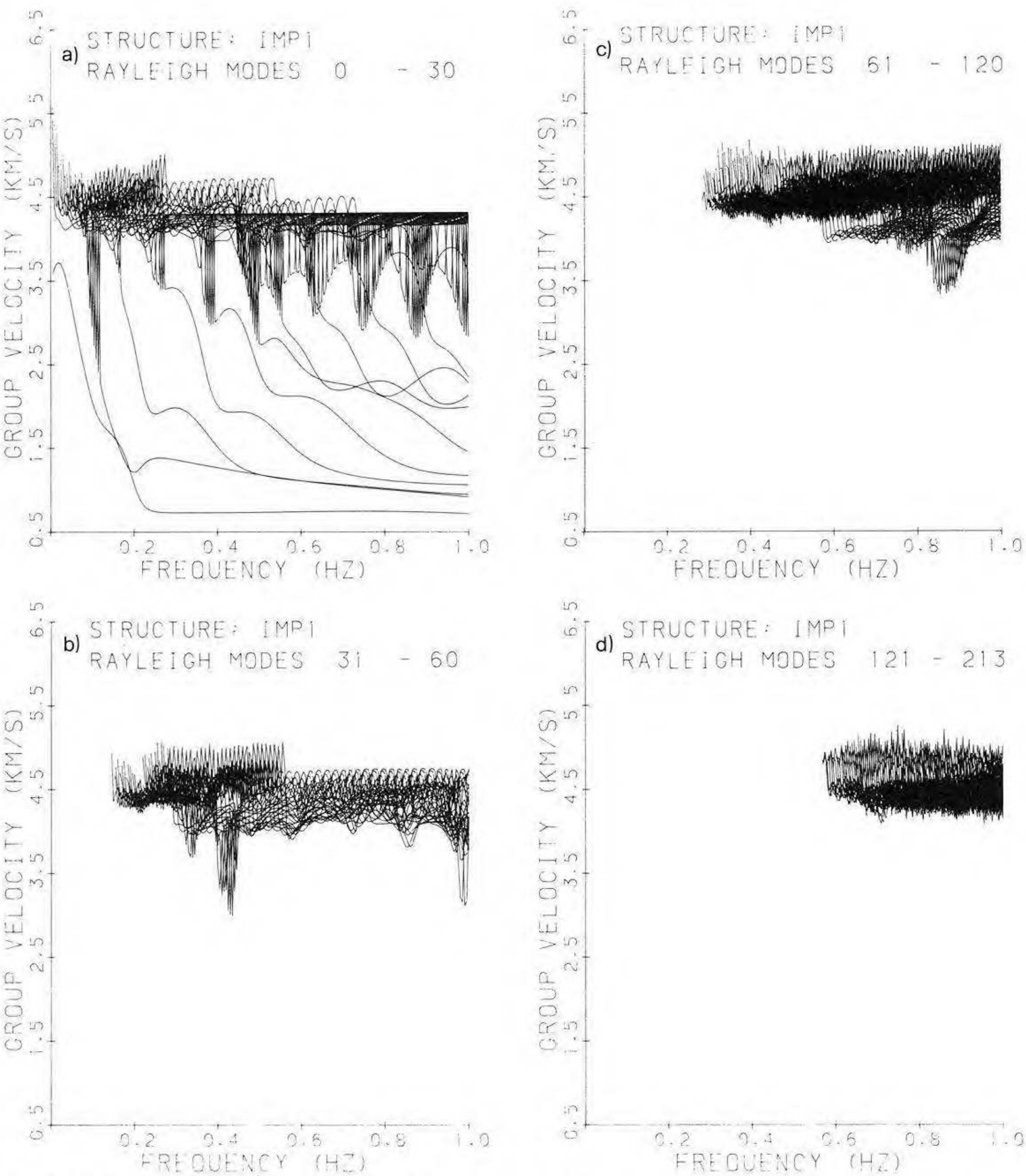

Fig. 4a–d. Rayleigh-wave group velocities for the continental structure

waves. The identification of these last phases (*Sn* and *Sb*) is also possible in Fig. 4b and c. In Figs. 4b–d, the highly oscillating portions of the group-velocity curves with values above 4.5 km/s can be associated with different body waves (either *P*-waves sampling the upper layers of *S*-waves sampling quite deep). A detailed analysis of this part of the group-velocity diagram allows a more precise identification. However, such an analysis is beyond the purpose of this paper.

For the oceanic model, similar observations can be made as far as the general properties of the group-velocity diagram is concerned (Figs. 5a–d). In general stationary phases corresponding to crustal waves, sedimentary waves and water waves are easily identified. The three families of waves, each of them formed by the combination of several higher modes are, in some cases, overlapping and they can be distinguished only on the basis of the group-velocity value they tend to. Thus, stationary portions of the group-velocity curves centred around 3.7 km/s are essentially crustal waves (3.7 km/s is the velocity of *S*-waves in the crustal layers), those centred around 1.0 km/s are essentially sedimentary waves (1.0 km/s is the velocity of *S*-waves in the sedimentary layer) and finally, those centred around 1.5 km/s can be associated with water waves (1.52 km/s is the velocity of *P*-waves in the water). Other stationary portions, visible in the group-velocity range 4.0–4.4 km/s, can be associated with *Sa*, *Sn* and *Li*. A more detailed analysis of these group-velocity spectra is given by Chiaruttini et al. (1985).

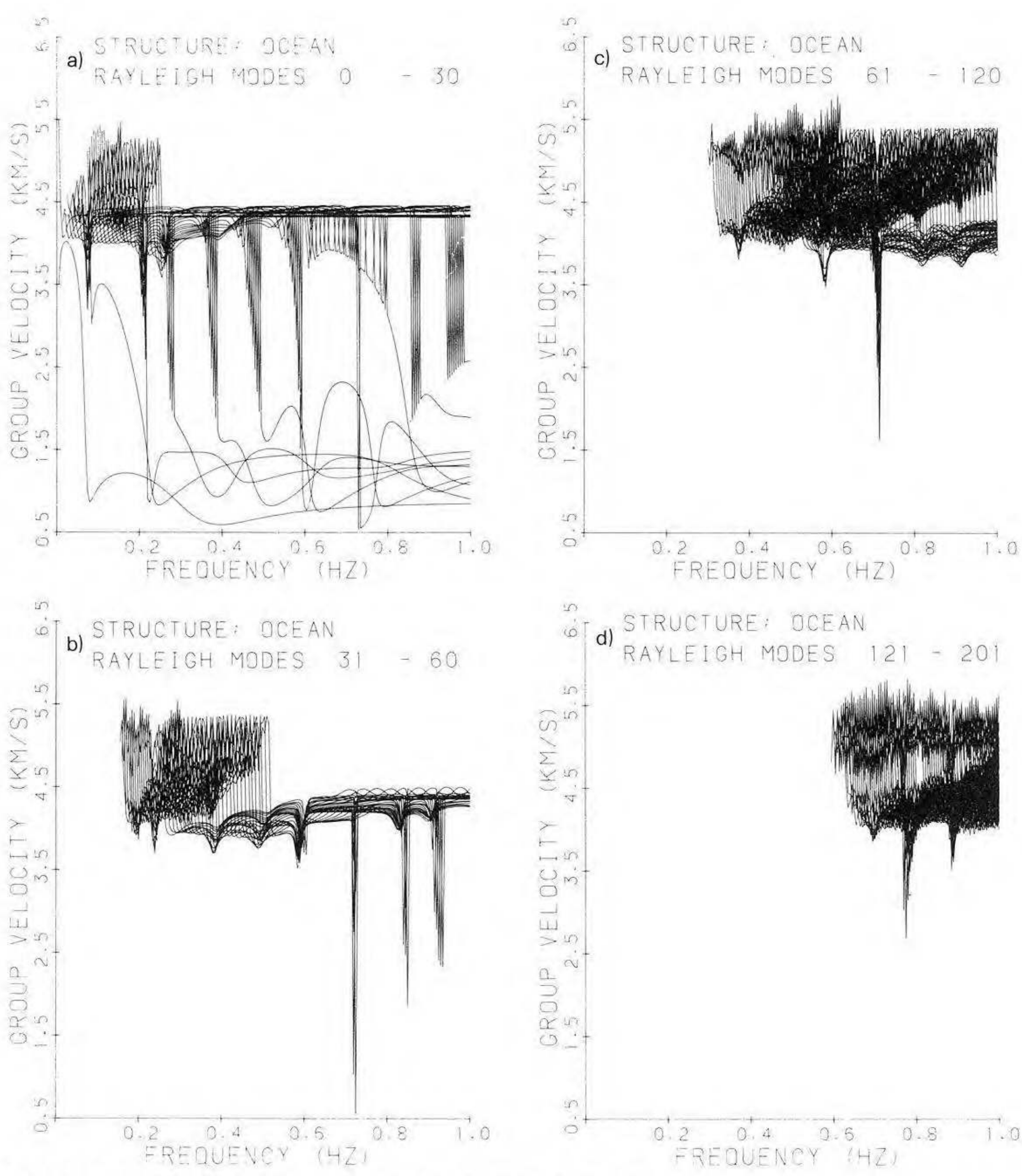

Fig. 5a–d. Rayleigh-wave group velocities for the oceanic structure

6.3. Energy integral

As for group velocities, a single plot of the energy integral I_1 is not suitable for interpretation. Thus, also in this case four plots have been made. Due to the large variations of the energy integral it is convenient to plot $\log I_1$. Figure 6a–d refers to the continental model, while Fig. 7a–d refers to the oceanic one. From Fig. 6a the effect of trapping in the upper-mantle low-velocity layer is clearly visible; in fact, in general, large values of I_1 correspond to practically no motion at the free surface, while small values of I_1 correspond to significant surface displacement. It is quite interesting to observe that for frequencies smaller than 0.08 Hz the fundamental dominates, while for larger frequencies (up to about 0.2 Hz) several higher modes are characterized by small values of I_1, i.e. are dominating. In the frequency range 0.15–0.20 Hz the fundamental and the first higher mode are the dominant ones, while for larger frequencies very many modes may contribute significantly to the surface displacement. As a general rule it can be stated that significant surface displacements may be expected from all the modes having I_1 values not exceeding 1,000. $(I_1)_{min}$, where $(I_1)_{min}$ indicates the absolute minimum value of I_1 at each frequency. For the case shown in the figure, significant surface displacement can be expected as long as $I_1 < 10^{10}$ kg/m^2. However, the exact prediction of the surface displacement from I_1 is not straightforward since it strongly depends upon many factors, as can be seen from Eq.

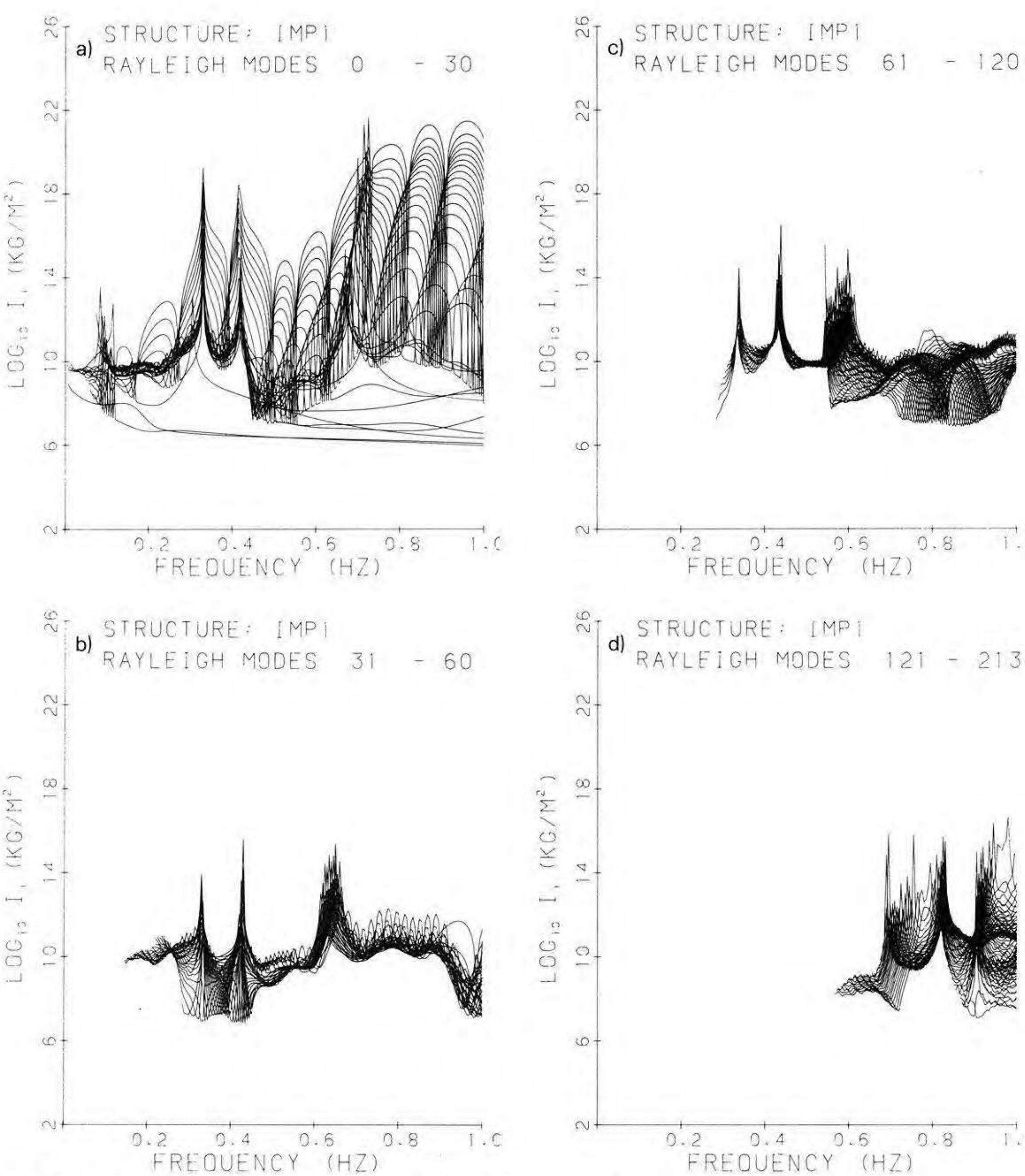

Fig. 6a–d. Rayleigh-wave energy integral, I_1, for the continental structure

(35). In Fig. 6b–d the trapping in the mantle low-velocity layer is not as visibly dramatic as for the first higher modes. This indicates that modes with high-order number are, in general, sampling the whole structure in a rather homogeneous way. On the other hand, a common feature of all parts of Fig. 6 are the very narrow peaks associated with the presence of sediments. If the source is located in the proximity of the sedimentary layers in correspondence with these narrow peaks and even if I_1 is quite large, one may expect significant surface motion mainly in the horizontal component; in fact, in these portions of the spectrum, the eigenfunctions are characterized by large lobes concentrated in the sedimentary layers and the ellipticity (see next section) gets very large. The sedimentary layers are also responsible for the fact that the fundamental mode is not dominant, i.e. does not have the smallest I_1 over the entire spectrum.

Figure 7a–d referring to the oceanic model can be analysed in the same way. In Fig. 7a, as it could be expected from the observations made when considering phase and group velocities, the presence of water and sedimentary layers introduces quite narrow peaks around frequencies of 0.08, 0.22, 0.40, 0.55, 0.70, 0.90 Hz superimposed on the broader peaks, due to the trapping in the upper-mantle low-velocity layer. In Fig. 7b the effect of the upper-mantle low-velocity layer is only visible for frequencies larger than 0.9 Hz, while the narrow peaks characterize the whole plot.

Before proceeding with the discussion of the main ingredients necessary for the costruction of synthetic seismograms, it is important to mention here a major

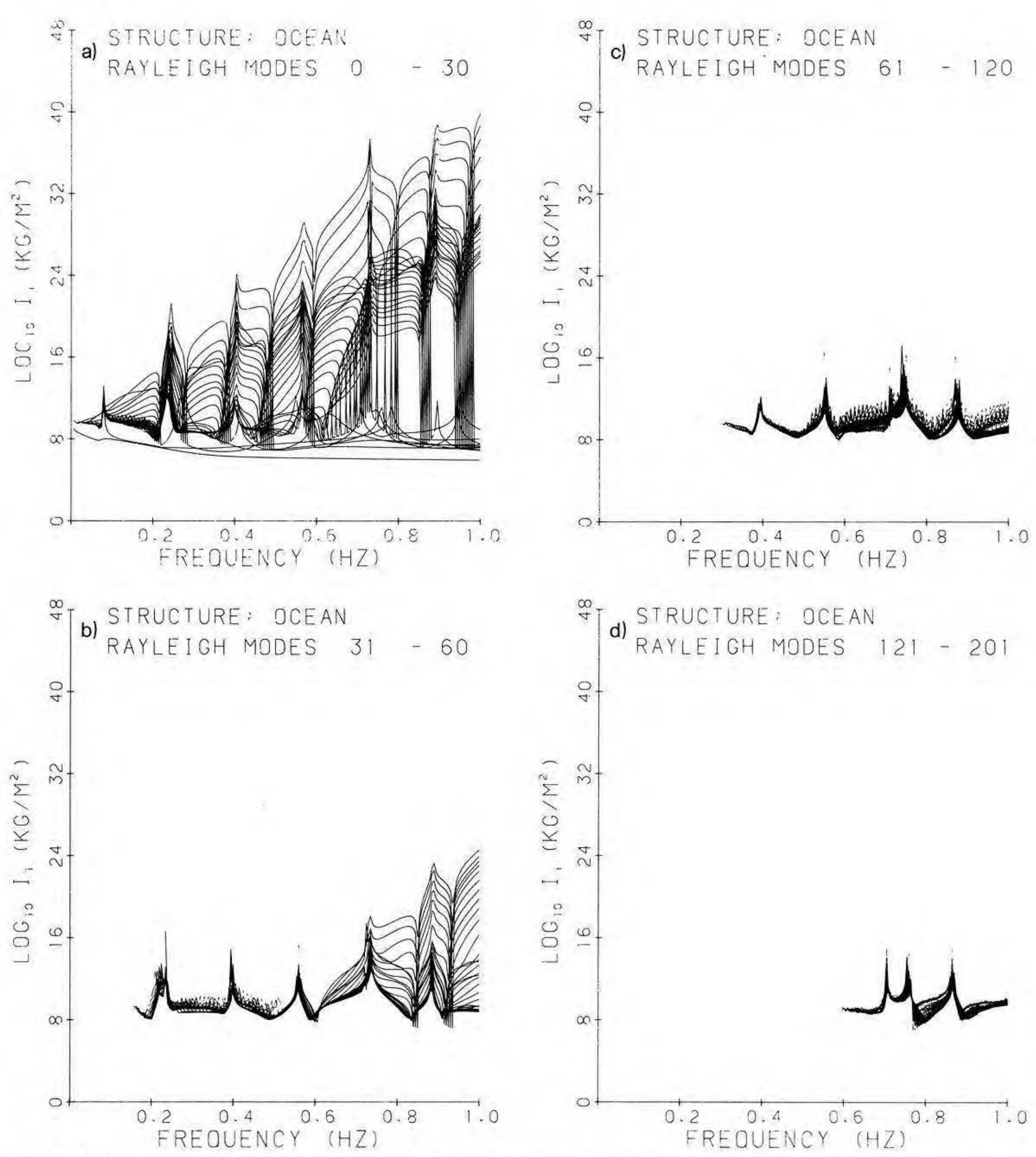

Fig. 7a–d. Rayleigh-wave energy integral, I_1, for the oceanic structure

point concerning the accuracy necessary in the computation of phase velocity to obtain correct values for I_1. As mentioned earlier, seven significant figures in phase-velocity determination are necessary to obtain three significant figures in group velocity. One could think that the same number of significant figures is sufficient to get accurate eigenfunctions. Unfortunately, this is not generally true and in some cases, mainly for large mode number, the precision required in phase-velocity determination is larger.

In Fig. 8 an example is given of the effect, on the computation of eigenfunctions, of the truncation of the eigenvalue to 13, 10, 9 and 8 figures respectively. The truncation to nine figures introduces already an undesirable extra swing at a depth of about 1,100 km; however, the integration versus depth of these eigenfunctions can still give accurate enough values. The situation is totally different when the phase velocity is truncated to eight figures. In fact, in this case, the extra swing around 1,100 km depth is the dominant feature and the integration versus depth of such eigenfunctions gives absolutely meaningless values. From the present experience it can be stated that an accuracy of nine–ten figures is generally sufficient to ensure the computation of I_1 with the necessary accuracy. Analogous considerations are applicable to the computation of I_3 and I_4.

6.4. Ellipticity

Another important quantity describing Rayleigh modes particle motion is the ellipticity $\varepsilon_0 = -u^*(0)/w(0)$, i.e. the ratio between the horizontal and vertical components

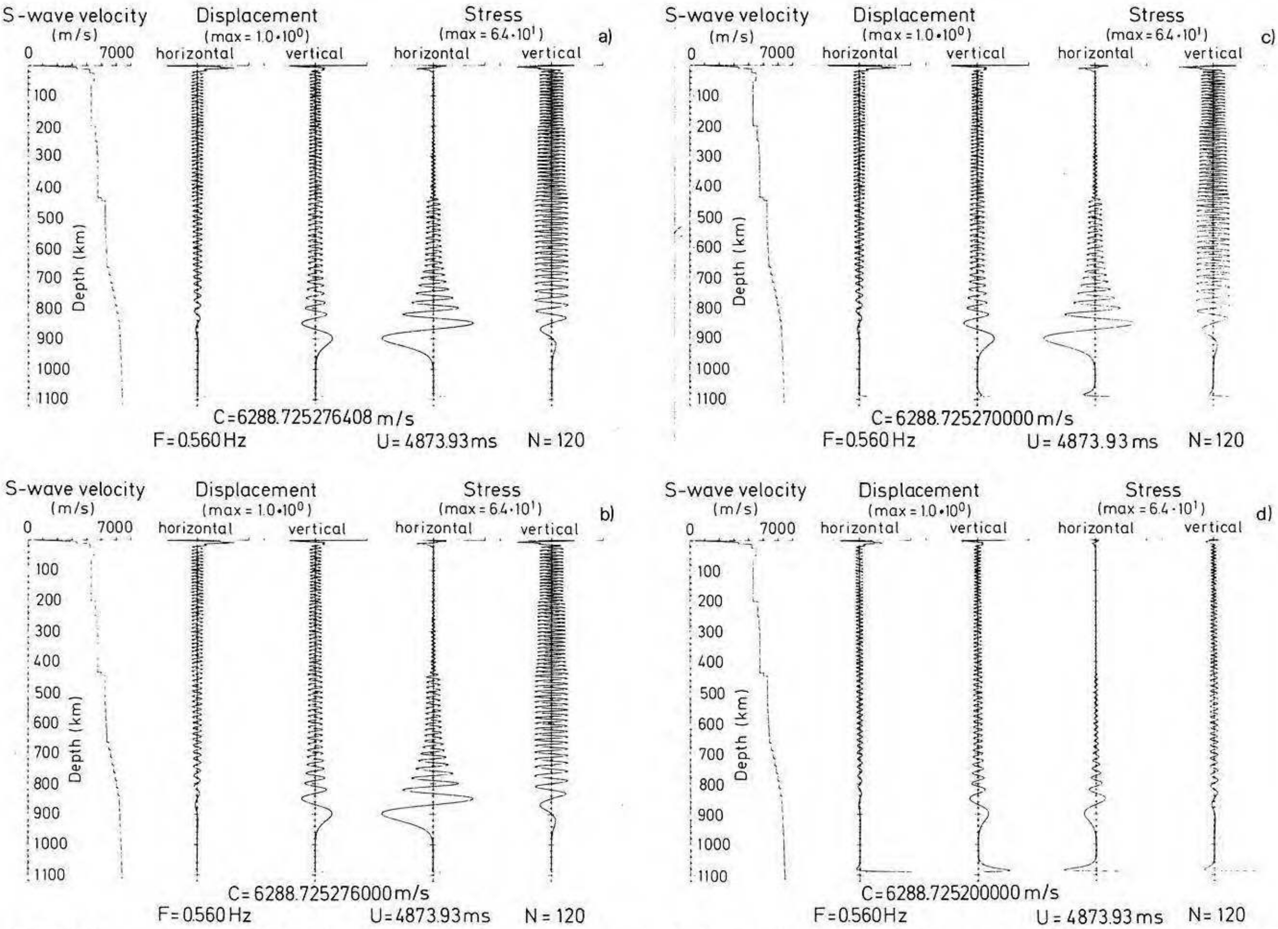

Fig. 8a–d. Example of the effect of truncating the precision of phase velocity in the determination of eigenfunctions for the higher mode number 120 at a frequency of 0.56 Hz for the continental structure: **a** phase velocity is determined with 13 figures; **b** phase velocity is determined with 10 figures; **c** phase velocity is determined with 9 figures; **d** phase velocity is determined with 8 figures. From the figure it is evident that nine–ten figures in phase velocity are necessary to ensure the correct computation of eigenfunctions

of motion at the free surface. It is very important to observe that while for the fundamental mode ε_0 is, in general, a smooth function of frequency, for the higher modes ε_0 can have abrupt discontinuities. More precisely, at some frequencies $\varepsilon_0 \rightarrow \pm\infty$ as a consequence of the fact that $w(0)$ passes through zero. This is not an obvious behaviour and strongly depends upon the elastic properties of the layers closest to the free surface. On the basis of tests performed up to now it can be stated that, for frequencies not exceeding 1 Hz and for Earth models without sedimentary layers, these discontinuities are present only once in a given mode and only for modes with large order number. On the contrary, if there are sediments at the top of the Earth models, several discontinuities are present also in each of the first higher modes. An example is given in Fig. 9 where, around 0.1, 0.3, 0.4, 0.7 and 0.9 Hz, for many modes $\varepsilon_0 \rightarrow \pm\infty$ as a consequence of the fact that $w(0)$ passes through zero at these frequencies.

The most interesting feature that can be observed here is that, due to the presence of sediments, the particle motion of several higher modes is essentially horizontal, i.e. $|\varepsilon_0| > 10$, over quite wide frequency ranges. A nice example is shown in Fig. 9a in the frequency bands around 0.3–0.4 Hz and 0.7–0.9 Hz. This is an extremely important observation which has several practical implications: for instance, in engineering seismology, the concentration of Rayleigh motion in the horizontal direction may play a relevant role in the so-called "amplification effect" introduced by sediments. Thus, sedimentary layers significantly increase the seismic hazard of a region as a consequence not only of the energy trapping, but also because they tend to make the horizontal component of motion of Rayleigh modes dominant (Chiaruttini et al., 1985). Very similar observations can be applied to the behaviour of ε_0 in the case of the oceanic structure as can be seen from Fig. 10 where, as an example, the ellipticity for the first 31 modes is shown.

6.5. Phase attenuation

For large frequencies, the phase attenuation of surface waves, C_2, can be related to the quality factor (Q_x), by the relation

$$1/(Q_x) = 2\, C_1\, C_2 \tag{34}$$

where C_1 and C_2 are defined in Sect. 5.

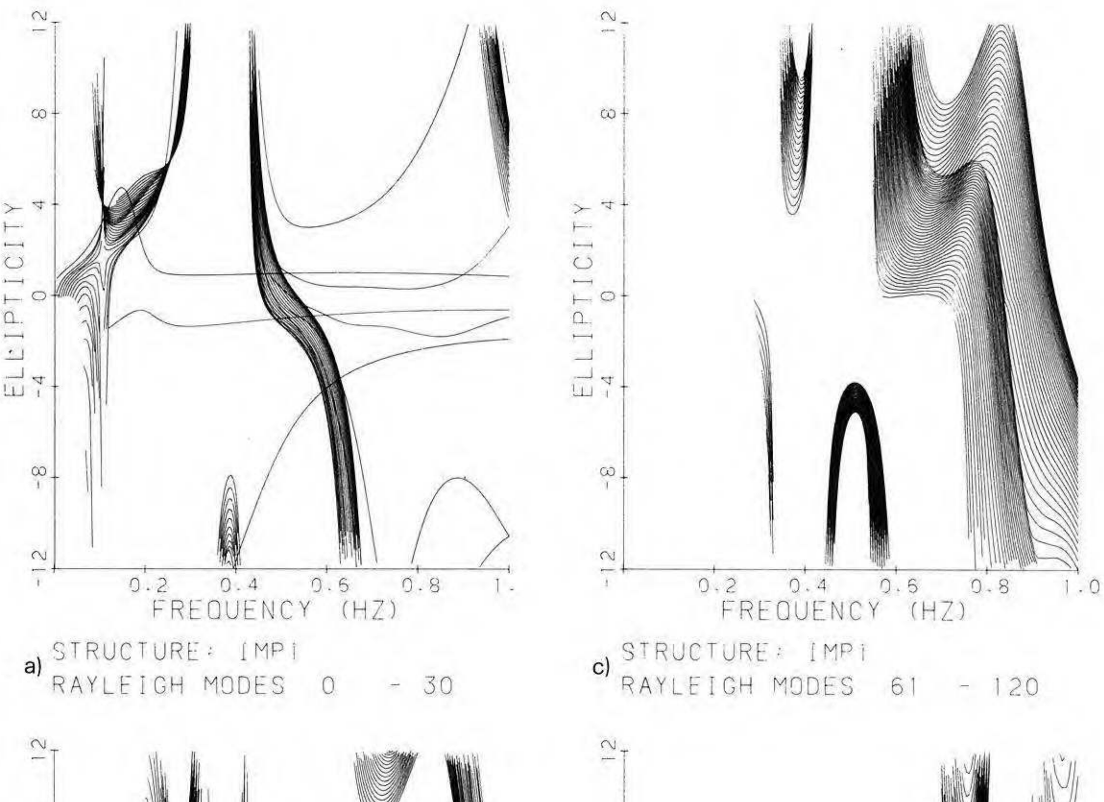

Fig. 9a–d. Ellipticity, ε_0, curves for the continental structure. The discontinuities quite clearly visible around 0.1, 0.3, 0.4, 0.7 and 0.9 Hz are due to the crossing of $w(0)$ through zero

Also for Rayleigh waves, the difference between the anelastic phase velocity C_1 and the perfectly elastic phase velocity c can be either positive or negative, as was already shown by Schwab and Knopoff (1971) for the first few modes of Love waves. For the considered continental model, the phase velocity correction due to anelasticity is in the range 0.0002–0.0006 km/s; this range seems to be quite representative for many cases. Thus, in the period range we have investigated, computations made for perfectly elastic layers are correct to at least four figures.

Also in this case, for reasons of clarity, it has been necessary to subdivide the plot of Q_x into four parts. Figure 11a gives the first 31 modes. Though it is practically impossible to follow individual modes in their entirety, it is relatively easy to see the effect of the layering of Q_α and Q_β. For instance, the fundamental mode shows a large peak around 0.05 Hz and this

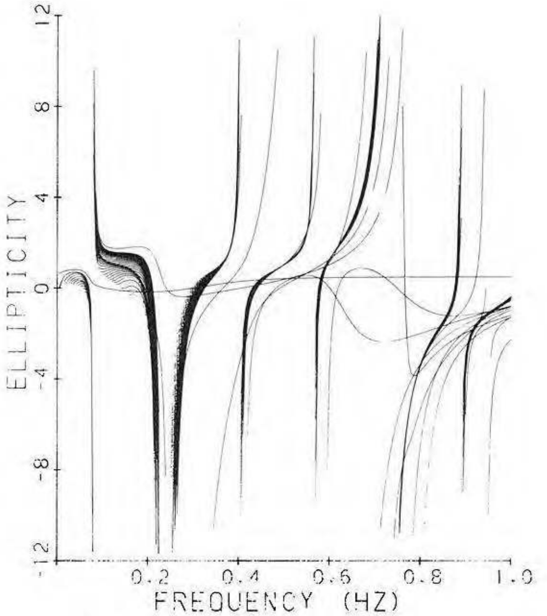

Fig. 10. Ellipticity, ε_0, curves for the first 31 modes of the oceanic structure. In this case also, the various discontinuities affecting each mode are due to the presence of the sedimentary layer

corresponds to wave propagation in the lower crust and upper mantle where $Q_\beta=450$. For frequencies larger than 0.15 Hz several modes are characterized by very low values and this indicates wave propagation in the upper sedimentary layers where Q_β does not exceed 100.

As a general remark, it can be observed that Q_x has a frequency dependence quite similar to that of group velocities; however, while group-velocity envelopes of crustal and sedimentary waves are quite continuous (Fig. 4a), a clear and obvious separation exists between Q_x values for waves propagating in the sediments and in the crust. In fact, crustal waves exhibit fairly large values of Q_x (200 and more) as a consequence of the high Q_β in the crust, while sedimentary waves exhibit rather low values of Q_x as a consequence of the low Q_β in the sediments.

The trapping in the asthenospheric low-velocity layer, characterized by $Q_\beta=100$, is clearly visible for several modes which get very close to each other and have almost constant Q_x, close to 100.

In Fig. 11b the low values of Q_x around 0.35 and 0.40 Hz correspond to sedimentary waves, while the high values of Q_x around 0.90 Hz correspond to crustal waves. In Fig. 11c still some effect of sediments is visible around 0.85 Hz. From the above considerations it turns out that in order to perform easily interpretable measurements of Q_x it is necessary to apply quite accurate time or group velocity windows to the records before any further processing. In fact, an indiscriminate use of amplitude spectra may lead to reasonable Q_x values which, however, can not be easily related to the anelastic properties of the studied area.

7. Computation of synthetic seismograms

Ben-Menahem and Harkrider (1964) developed the formalism necessary for the study of point sources in multilayered media. A detailed description of the fault model of an earthquake used in the following computations is given by Panza et al. (1973). Accordingly in the reference system shown in Fig. 12, the asymptotic expression of the Fourier time transform of the j-th Rayleigh-mode displacement at the free surface of perfectly elastic Earth models, at distance r from the source, can be written

$$\begin{aligned} U_r^{DC} &= \{|R(\omega)| \exp(i\phi_0)\} |\mathbf{n}| k^{\frac{1}{2}} \exp(-i3\pi/4) \chi(\theta,h) \\ &\quad \varepsilon_0 A \exp(-ikr)/\sqrt{(2\pi r)} \\ U_z^{DC} &= [\varepsilon_0 \exp(i\pi/2)]^{-1} U_r^{DC} \\ U_\theta^{DC} &= 0 \end{aligned} \tag{35}$$

where $R(\omega)$ is the Fourier transform of the equivalent point-force time function, the quantity $\mathbf{n}$ is the unit vector perpendicular to the fault and has units of length,

$$\phi_0 = \arg R(\omega) \tag{36}$$

is the initial phase, k is the wavenumber,

$$\varepsilon_0 = -\frac{u^*(0)}{w(0)} \tag{37}$$

and $w(\zeta)$ and $u^*(\zeta)$ are the vertical and horizontal components of displacement at depth ζ for 'plane' propagating Rayleigh waves (Haskell, 1953). The factor A is given by

$$A^{-1} = 2cu \int_0^\infty \xi(\zeta)\, d\zeta \tag{38}$$

where c is the phase velocity, u is the group velocity,

$$\xi(\zeta) = \rho(\zeta)\, [u^*(\zeta)^2 + w(\zeta)^2]/w(0)^2 \tag{39}$$

and ρ is the density. The azimuthal dependence of the response is given by

$$\chi(\theta,h) = d_0 + i(d_1 \sin\theta + d_2 \cos\theta) + d_3 \sin 2\theta + d_4 \cos 2\theta. \tag{40}$$

The quantities d_i are

$$\begin{aligned} d_0 &= \tfrac{1}{2}\sin\lambda \sin 2\delta\, B(h), \\ d_1 &= -\sin\lambda \cos 2\delta\, C(h), \\ d_2 &= -\cos\lambda \cos\delta\, C(h), \\ d_3 &= \cos\lambda \sin\delta\, A(h), \\ d_4 &= -\tfrac{1}{2}\sin\lambda \sin 2\delta\, A(h), \end{aligned} \tag{41}$$

with

$$\begin{aligned} A(h) &= -\frac{u^*(h)}{w(0)}, \\ B(h) &= -\left[3 - 4\frac{\beta(h)^2}{\alpha(h)^2}\right]\frac{u^*(h)}{w(0)} - \frac{2}{\rho(h)\,\alpha(h)^2}\,\frac{\sigma^*(h)}{\dot{w}(0)/c}, \\ C(h) &= -\frac{1}{\mu(h)}\,\frac{\tau(h)}{\dot{w}(0)/c}. \end{aligned} \tag{42}$$

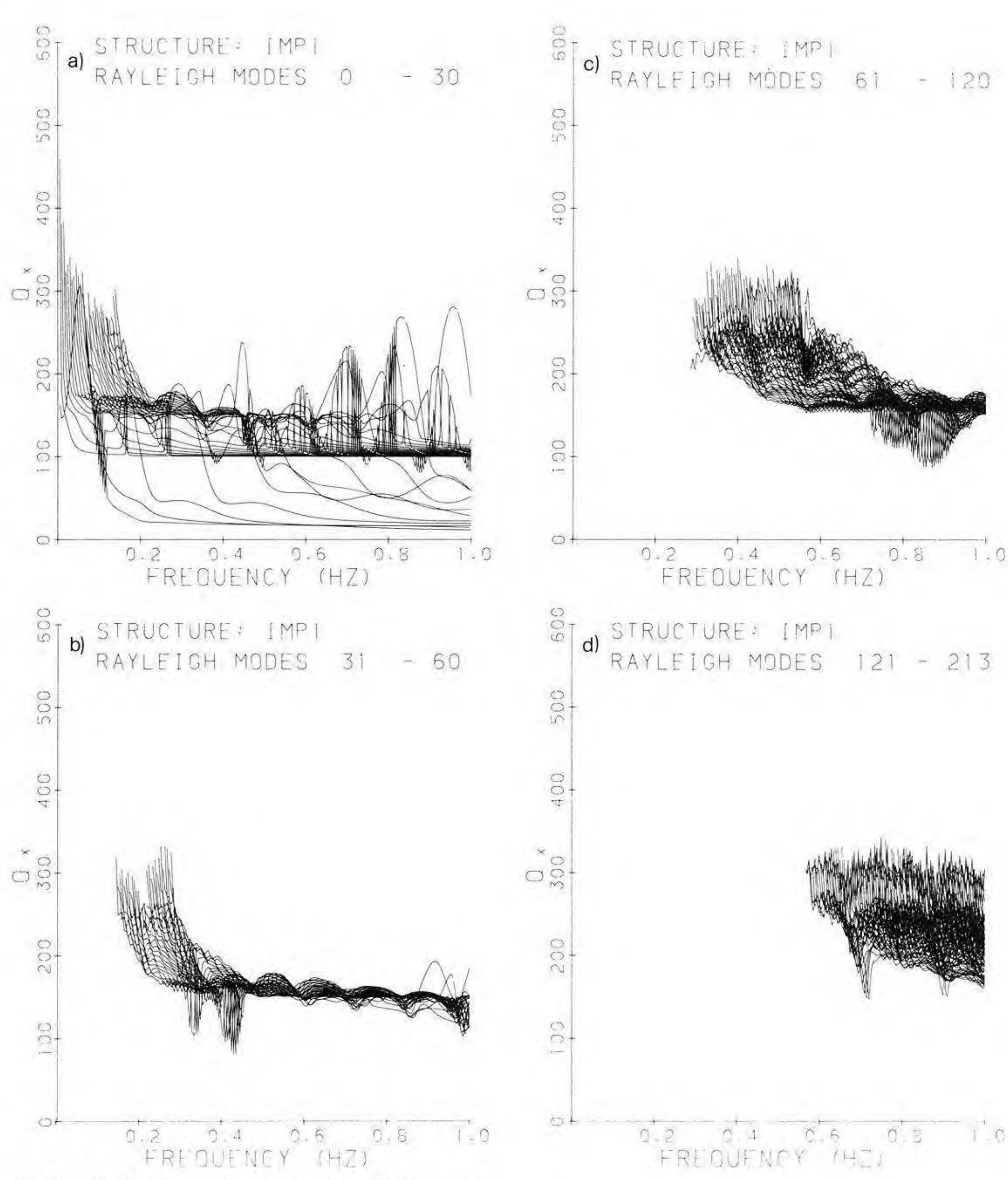

Fig. 11a–d. Q_x curves for the continental structure

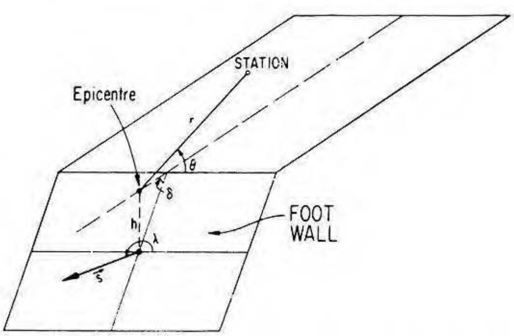

Fig. 12. Source geometry and coordinate system associated with free surface: θ is the angle between the strike of the fault and the epicentre-station direction, δ is the dip angle and λ is the rake angle, h is the source depth

If one adopts the far-field relation given by Ben-Menahem and Harkrider (1964):

$$\frac{U_r}{U_z} = \varepsilon_0 \, e^{i\pi/2}, \tag{43}$$

then for a wave propagating in the positive r direction with retrograde elliptical particle motion, U_r leads U_z by $\pi/2$ radians and ε_0 is positive only if z is chosen to increase upward. If, however, as in Panza et al. (1972), Haskell (1953) and the first part of Harkrider (1964), z is chosen positive downward, U_r leads U_z by $3\pi/2$ radians. If relation (43) is used to define ε_0, in this latter case retrograde particle motion is defined by negative values of the ellipticity. Relative to the formalism given

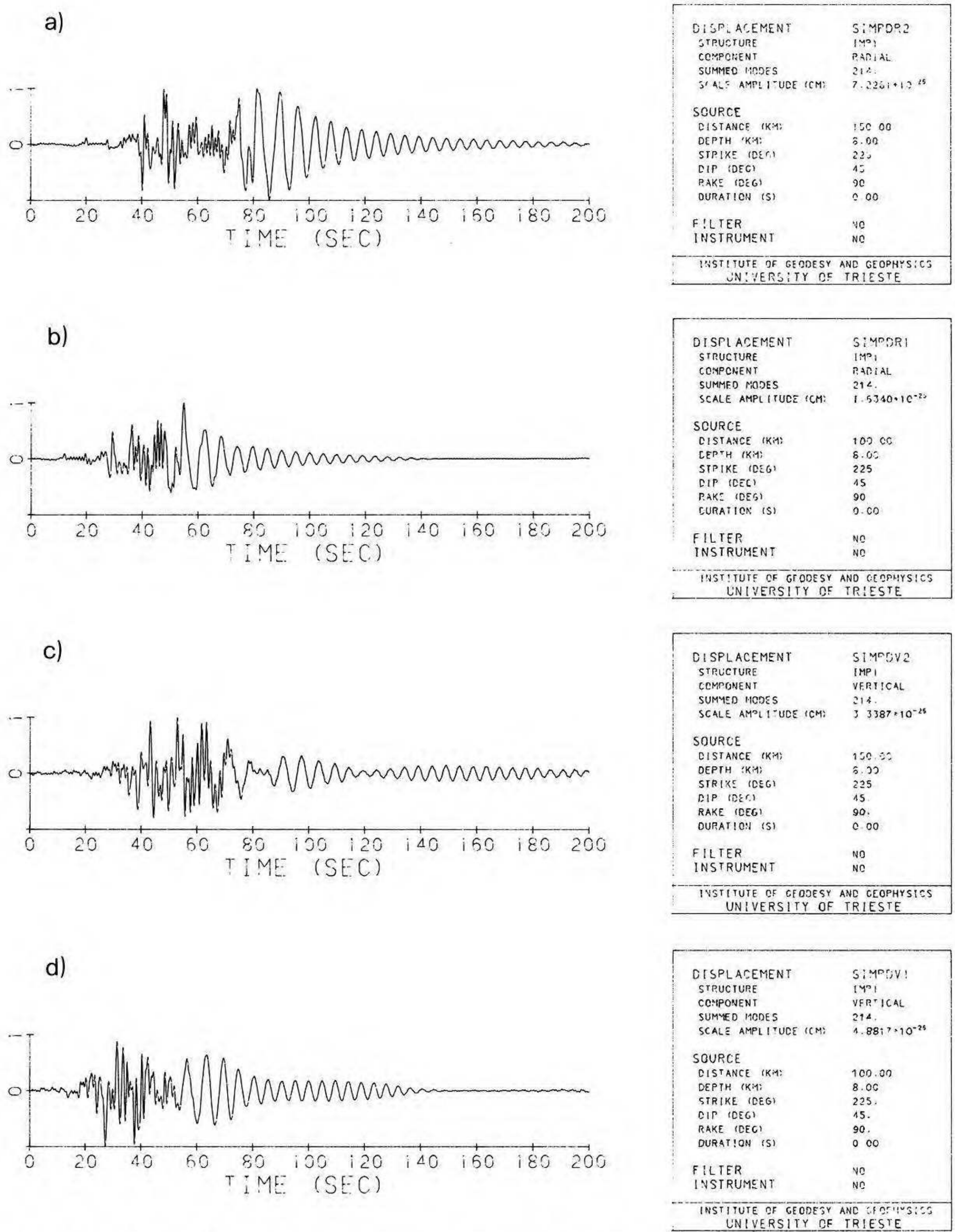

Fig. 13a–d. Examples of synthetic seismograms computed for the continental structure for dip-slip point sources

by Ben-Menahem and Harkrider (1964), the following observation is relevant in programming. As stated above, U_r leads U_z by $\pi/2$ radians, which corresponds to U_z and z being positive in the upward direction. However, the depth-dependent quantities $u^*(h)/w(0)$, $w(h)/w(0)$, $\sigma^*(h)/w(0)/c$ and $\tau(h)/w(0)/c$ are to be computed from the usual Haskell (1953) formalism, in which z is positive in the downward direction.

The asymptotic expression just described allows the computation of synthetic seismograms with at least three significant figures as long as $kr \geqq 10$ (Panza et al., 1973).

When considering anelastic models, the wavenumber k becomes complex

$$k = (\omega/C_1) - i\,\omega\,C_2.$$

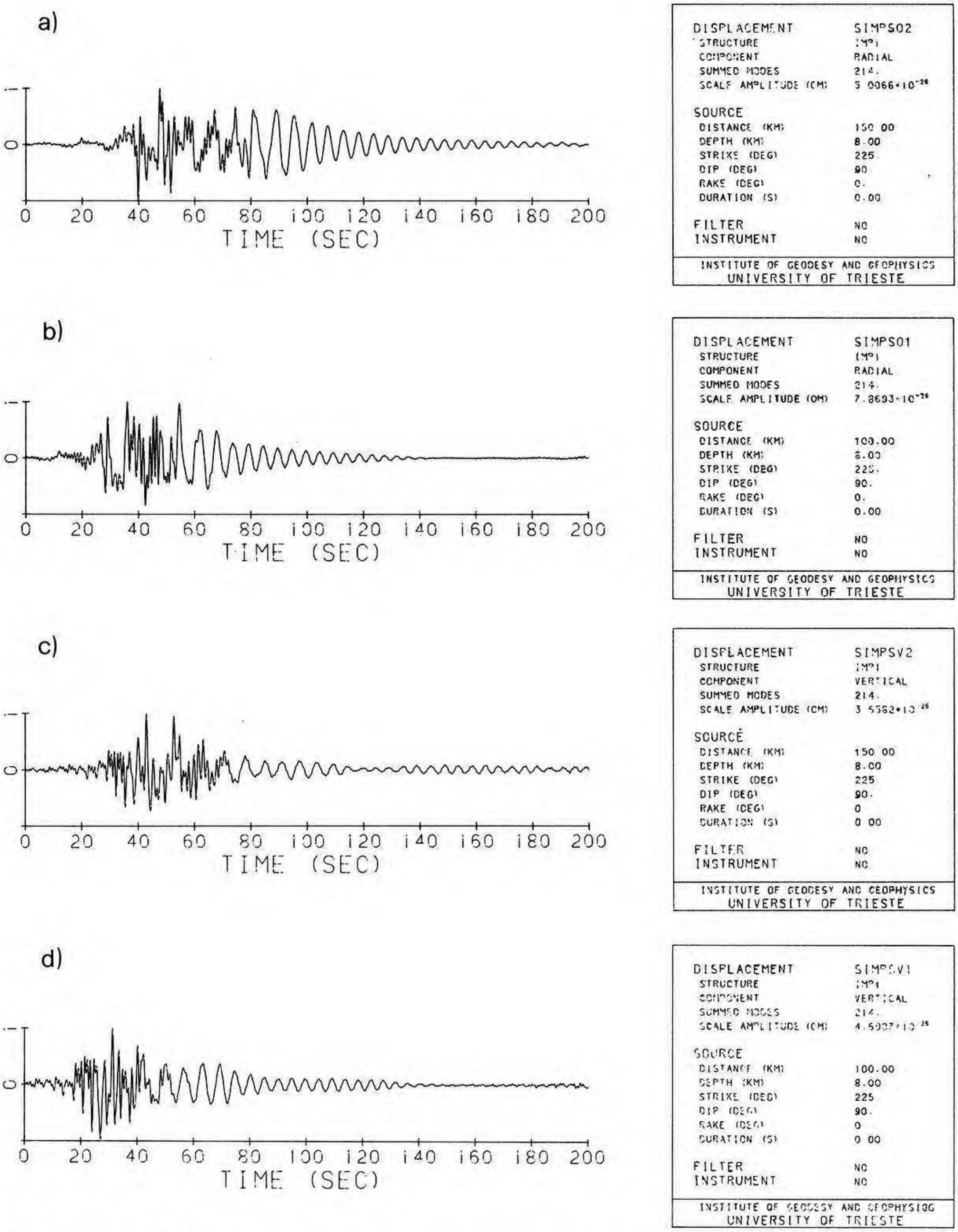

Fig. 14a–d. Examples of synthetic seismograms computed for the continental structure for strike-slip point sources

Thus the term $\exp(-ikr)$ can be written as

$$\exp(-i\omega r/C_1)\exp(-\omega C_2 r).$$

The term $e^{-\omega C_2 r}$, representing the amplitude damping is the main term introduced by anelasticity. Smaller effects, like those arising from complex group velocities and eigenfunctions are not included in the present calculations.

The extension of these results to the available formalism for sources with finite dimensions and duration (e.g. Ben-Menahem, 1961; Kanamori and Given, 1981; Stewart and Kanamori, 1982) is quite straightforward.

It is quite important to observe that the expressions for sources of finite dimensions are also valid in the far-field approximation, which can be roughly expressed by the condition that the source-receiver distance must be an order of magnitude greater than source dimensions. If this condition is not satisfied while the condition $kr \geqq 10$ still holds, the synthetic signal can be constructed as a proper sum of seismograms given by point sources separated in time and space. With the modal approach this is easily done. In fact, following this method, for a given Earth model, different seismograms corresponding to different sources, can be computed with very little computer time; essentially the time required for a Fast Fourier transform, since all the time-consuming computations (eigenvalues and eigenfunctions) are independent of source specifications.

Some examples of computations of synthetic seismograms, for point sources with $R(\omega)$ equal to a unit step function and for the continental model shown in Table 1, are given in Figs. 13 and 14. Parts *a* and *c* of Fig. 13 give, respectively, the radial and vertical component of motion at a distance of 150 km from a source of dip-slip type. It is important to observe that the radial component is more than twice the vertical one, and this is in quite good agreement with what has been observed about the ellipticity in Sect. 6.4. Similar considerations apply to Fig. 13b and d, where synthetic seismograms computed for an epicentral distance of 100 km are shown.

From these synthetic seismograms it is easy to see the large increment of the duration of the signal with increasing distance, mainly due to the dispersion of the fundamental and first few higher modes. In Fig. 14 examples for strike-slip point-sources are given which essentially confirm the previous observations. From a comparison of Fig. 13a with Fig. 14a it turns out, quite evidently, how difficult it can be to distinguish among the two mechanisms if the analysis is limited to the first part of the record, while significant differences can be seen in the records for a time greater than 60 s. On the other hand, the difference between Fig. 13b and Fig. 14b is really very small over the entire duration. The same considerations can be applied to the vertical component of motion.

A more detailed discussion of synthetic seismograms, computed using the technique described in this paper and some comparisons with experimental data is given by Suhadolc and Panza (1985).

8. Conclusions

The stage reached in the development of algorithms for the computation of eigenvalues and eigenfunctions of Rayleigh waves for flat layered anelastic models of the Earth allows "complete" synthetic seismograms to frequencies as high as 1 Hz to be constructed, with satisfactory efficiency. Routinely, it is possible to consider Earth models made up of 70 layers and more. Thus, it is feasible also to model any sort of gradient in the distribution versus depth of elastic and anelastic properties by a rather fine layering. Typical CPU times for the frequency-domain computations on an IBM 370/168 computer are around 1 h, while the construction of the time series requires about 300 s. This last figure decreases to only 30 s for all subsequent seismograms computed for different sources, located at the same depth.

Very preliminary attempts made using the vector computer CRAY-1 gave characteristic times about ten times smaller for all computations. This very interesting result could be further improved via an optimization of the code to the vector machine. This task is presently in progress.

Acknowledgements. I am extremely grateful to Dr. F. Schwab for his very important help during the development of the present research. I have very much appreciated the encouraging comments and suggestions of Prof. L. Knopoff and Prof. B.A. Bolt. The frequent discussions with Dr. C. Chiaruttini, Dr. G. Costa, Prof. I. Marson and Dr. P. Suhadolc were very useful in giving the manuscript its final form, which was critically read by Dr. A. Cichowicz and whom I thank very deeply.

Special thanks go to Mrs. I. Galante for the patient and accurate typing of the manuscript and to Mr. M. Gergolet and Mr. S. Zidarich for their help in elaborating the diagrams.

This research has been performed with financial support of CNR (Grants 83.02248, 83.02432) and MPS (60% and 40%).

References

Aki, K., Richards, P.G.: Quantitative seismology. Theory and methods. San Francisco: W.H. Freeman and Co. 1980

Ben-Menahem, A.: Radiation of seismic surface waves from finite moving sources. Bull. Seismol. Soc. Am. **51**, 401–435 1961

Ben-Menahem, A., Harkrider, D.G.: Radiation patterns of seismic surface waves from buried dipolar point sources in a flat stratified Earth. J. Geophys. Res. **69**, 2605–2620, 1964

Brune, J.N.: Attenuation of dispersed wave trains. Bull. Seismol. Soc. Am. **52**, 109–112, 1962

Calcagnile, G., Panza, G.F.: Vertical and SV components of Sa. Geophys. J. R. Astron. Soc. **38**, 317–325, 1974

Chiaruttini, C., Costa, G., Panza, G.F.: Wave propagation in multilayered media: The effect of waveguides in oceanic and continental Earth models. J. Geophys. **58**, 189–196, 1985

Cuscito, M., Panza, G.F.: Determinazione simultanea del momento sismico e dei parametri strutturali usando sismogrammi sintetici completi. Rend. Soc. Geol. It. **4**, 477–478, 1981

Dunkin, J.W.: Computation of modal solutions in layered elastic media at high frequencies. Bull. Seismol. Soc. Am. **55**, 335–358, 1965

Futtermann, W.: Dispersive body waves. J. Geophys. Res. **67**, 5279–5291, 1962

Harkrider, D.G.: Surface waves in multilayered elastic media. 1. Rayleigh and Love waves from buried sources in a multilayered elastic half-space. Bull. Seismol. Soc. Am. **54**, 627–679, 1964

Harvey, D.J.: Seismograms synthesis using normal mode superposition: the locked mode approximation. Geophys. J. R. Astron. Soc. **66**, 37–69, 1981

Haskell, N.A.: The dispersion of surface-waves on multilayered media. Bull. Seismol. Soc. Am. **43**, 17–34, 1953

Kanamori, H., Given, J.W.: Use of long-period surface wave for rapid determination of earthquake-source parameters. Phys. Earth Planet. Int. **27**, 8–31, 1981

Kennett, B.L.N.: Seismic wave propagation in stratified media. Cambridge: Cambridge University Press 1983

Kerry, N.J.: Synthesis of seismic surface waves. Geophys. J. R. Astron. Soc. **64**, 425–446, 1981

Knopoff, L.: A matrix method for elastic wave problems. Bull. Seismol. Soc. Am. **54**, 431–438, 1964a

Knopoff, L.: Q. Rev. Geophys. **2**, 625–660, 1964b

Knopoff, L., Aki, K., Archambeau, C.B., Ben-Menahem, A., Hudson, J.A.: Attenuation of dispersed waves. J. Geophys. Res. **69**, 1655–1657, 1964

Liao, A., Schwab, F., Mantovani, E.: Computation of complete theoretical seismograms for torsional waves. Bull. Seismol. Soc. Am. **68**, 317–324, 1978

Mueller, S.: A new model of the continental crust. In: The Earth's crust, J. Heacock ed.: pp. 289–317, A.G.U., Monogr. 20, 1977

O'Connell, R.J., Budiansky, B.: Measure of dissipation in viscoelastic media. Geophys. Res. Lett. **5**, 5–8, 1978

Panza, G.F.: Evolution of the Earth's lithosphere. In: Mechanisms of continental drift and plate Tectonics, P.A. Davies and S.K. Runcorn eds.: pp. 75–87. Academic Press 1980

Panza, G.F., Calcagnile, G.: Lg, Li and Rg from Rayleigh modes. Geophys. J. R. Astron. Soc. **40**, 475–487, 1974

Panza, G.F., Cuscito, M.: Influence of focal mechanism on shape of isoseismals: Irpinia earthquake of November 23, 1980 Pure Appl. Geophys. **120**, 577–582, 1982

Panza, G.F., Schwab, F., Knopoff, L.: Channel and crustal Rayleigh waves. Geophys. J. R. Astron. Soc. **30**, 273–280, 1972

Panza, G.F., Schwab, F., Knopoff, L.: Multimode surface waves for selected focal mechanisms. I. Dip-slip on a vertical fault plane. Geophys. J. R. Astron. Soc. **34**, 265–278, 1973

Pekeris, C.L.: Theory of propagation of explosive sound in shallow water. Geol. Soc. Am. Mem. **27**, 1–116, 1948

Pestel, E.C., Leckie, F.A.: Matrix methods in elastomechanics. New York: McGraw-Hill 1963

Schwab, F.: Surface-wave dispersion computations: Knopoff's method. Bull. Seismol. Soc. Am. **60**, 1491–1520, 1970

Schwab, F., Knopoff, L.: Surface waves on multilayered anelastic media. Bull. Seismol. Soc. Am. **61**, 893–912, 1971

Schwab, F., Knopoff, L.: Fast surface wave and free mode computations. In: Methods in computational physics, Vol. 11. B.A. Bolt, ed.: pp. 87–180. New York: Academic Press 1972

Schwab, F., Knopoff, L.: Love waves and the torsional free modes of a multilayered anelastic sphere. Bull. Seismol. Soc. Am. **63**, 1107–1117, 1973

Schwab, F., Nakanishi, K., Cuscito, M., Panza, G.F., Liang, G., Frez, J.: Surface-wave computations and the synthesis of theoretical seismograms at high frequencies. Bull. Seismol. Soc. Am. 1984 (in press)

Schwab, F., Cuscito, M., Panza, G.F., Nakanishi, K.: Surface-wave computations and the synthesis of theoretical seismograms at high frequency. II. Group velocity, attenuation due to anelasticity and frequency intervals. In preparation, 1985

Stewart, G.S., Kanamori, H.: Complexity of rupture in large strike-slip earthquakes in Turkey. Phys. Earth Planet. Int. **28**, 70–84, 1982

Suhadolc, P., Panza, G.F.: Some applications of seismosynthesis through the summation of modes of Rayleigh waves. J. Geophys. **58**, 183–188, 1985

Suhadolc, P., Panza, G.F., Cuscito, M., Schwab, F.: Fully automatic computation of synthetic seismograms for P-SV motion in 1 Hz. In preparation, 1985

Takeuchi, H., Saito, M.: Seismic surface wave. In: Methods in computational physics, Vol. 11, B.A. Bolt, ed.: pp. 217–295. New York: Academic Press 1972

Thomson, W.T.: Transmission of elastic waves through a stratified solid medium. J. Appl. Phys. **21**, 89–93, 1950

Thrower, E.N.: The computation of dispersion of elastic waves in layered media. J. Sound. Vib. **2**, 210–226, 1965

Watson, T.H.: A note on fast computation of Rayleigh wave dispersion in the multilayered half-space. Bull. Seismol. Soc. Am. **60**, 161–166, 1970

Woodhouse, J.H.: The joint inversion of seismic wave forms for lateral variations in Earth structure and earthquake source parameters. In: Earthquakes: Observations, theory and interpretation, H. Kanamori and E. Boschi, eds. Amsterdam: North-Holland Publ. Co 1983

Received February 26, 1985; revised version May 20, 1985
Accepted July 3, 1985